Cerebral Cortex, 2021;00: 1–23

doi: 10.1093/cercor/bhab040
Original Article

ORIGINAL ARTICLE

Microscale Physiological Events on the Human Cortical Surface

Angelique C. Paulk[1], Jimmy C. Yang[1,2], Daniel R. Cleary[3,4,5], Daniel J. Soper[1], Milan Halgren[1,6], Alexandra R. O'Donnell[1], Sang Heon Lee[7], Mehran Ganji[7], Yun Goo Ro[7], Hongseok Oh[7], Lorraine Hossain[8], Jihwan Lee[7], Youngbin Tchoe[7], Nicholas Rogers[4], Kivilcim Kiliç[3], Sang Baek Ryu[2], Seung Woo Lee[2], John Hermiz[7], Vikash Gilja[7], István Ulbert[9,10], Daniel Fabó[11], Thomas Thesen[12,13], Werner K. Doyle[13], Orrin Devinsky[13], Joseph R. Madsen[14], Donald L. Schomer[15], Emad N. Eskandar[2,16], Jong Woo Lee[17], Douglas Maus[1], Anna Devor[3], Shelley I. Fried[2,18], Pamela S. Jones[2], Brian V. Nahed[2], Sharona Ben-Haim[5], Sarah K. Bick[2], Robert Mark Richardson[2], Ahmed M. Raslan[19], Dominic A. Siler[19], Daniel P. Cahill[2], Ziv M. Williams[2], G. Rees Cosgrove[20], Shadi A. Dayeh[5,8,21] and Sydney S. Cash[1]

[1]Department of Neurology, Massachusetts General Hospital, Boston, MA 02114, USA, [2]Department of Neurosurgery, Massachusetts General Hospital, Boston, MA 02114, USA, [3]Departments of Neurosciences and Radiology, University of California San Diego, La Jolla, CA 92093, USA, [4]Department of Physics, University of California San Diego, La Jolla, CA 92093, USA, [5]Department of Neurosurgery, University of California San Diego, La Jolla, CA 92093, USA, [6]McGovern Institute for Brain Research and Department of Brain and Cognitive Sciences, Massachusetts Institute of Technology, Cambridge, MA 02139, USA, [7]Department of Electrical and Computer Engineering, University of California San Diego, La Jolla, CA 92093, USA, [8]Materials Science and Engineering Program, University of California San Diego, La Jolla, CA 92093, USA, [9]Research Centre for Natural Sciences, Institute of Cognitive Neuroscience and Psychology, 1519 Budapest, Hungary, [10]Pázmány Péter Catholic University, Faculty of Information Technology and Bionics, H-1444 Budapest, Hungary, [11]Epilepsy Centrum, National Institute of Clinical Neurosciences, 1145 Budapest, Hungary, [12]Department of Biomedical Sciences, University of Houston College of Medicine, Houston, TX 77204, USA, [13]Comprehensive Epilepsy Center, New York University School of Medicine, New York City, NY 10016, USA, [14]Departments of Neurosurgery, Boston Children's Hospital and Harvard Medical School, Boston, MA 02115, USA, [15]Department of Neurology, Beth Israel Deaconess Medical Center, Boston, MA 02215, USA, [16]Present address: Albert Einstein College of Medicine, Montefiore Medical Center, Department of Neurosurgery, Bronx, NY 10467, USA, [17]Department of Neurology, Brigham and Women's Hospital, Boston, MA 02115, USA, [18]Boston VA Healthcare System, 150 South Huntington Avenue, Boston, MA 02130, USA, [19]Department of Neurological Surgery, Oregon Health and Science University, Portland, OR 97239, USA, [20]Department of Neurosurgery, Brigham and

Women's Hospital, Boston, MA 02115, USA and [21]Department of Nanoengineering, University of California San Diego, La Jolla, CA 92093, USA

Address correspondence to Angelique C. Paulk. Email: apaulk@mgh.harvard.edu.

Abstract

Despite ongoing advances in our understanding of local single-cellular and network-level activity of neuronal populations in the human brain, extraordinarily little is known about their "intermediate" microscale local circuit dynamics. Here, we utilized ultra-high-density microelectrode arrays and a rare opportunity to perform intracranial recordings across multiple cortical areas in human participants to discover three distinct classes of cortical activity that are not locked to ongoing natural brain rhythmic activity. The first included fast waveforms similar to extracellular single-unit activity. The other two types were discrete events with slower waveform dynamics and were found preferentially in upper cortical layers. These second and third types were also observed in rodents, nonhuman primates, and semi-chronic recordings from humans via laminar and Utah array microelectrodes. The rates of all three events were selectively modulated by auditory and electrical stimuli, pharmacological manipulation, and cold saline application and had small causal co-occurrences. These results suggest that the proper combination of high-resolution microelectrodes and analytic techniques can capture neuronal dynamics that lay between somatic action potentials and aggregate population activity. Understanding intermediate microscale dynamics in relation to single-cell and network dynamics may reveal important details about activity in the full cortical circuit.

Key words: auditory stimulation, electrical stimulation, extracellular activity, human cortex, microelectrode

Introduction

Using neural recordings to uncover how the brain and underlying circuitry support behavior has traditionally concentrated on two ends of a spectrum detected with extracellular recordings: single-cell spiking activity or local field potentials (LFPs) arising from the summation of activity in large populations of neurons. However, other neural electrical signals, such as sodium or calcium potentials in the dendritic arbor, back-propagating action potentials, axonal action potentials, ephaptic signaling, and more, can be captured using intracellular recordings from single cells or optical imaging. Though neuroscience has investigated these other neural electrical signals, due to technical limitations, they have been difficult to study in vivo with large-scale circuit analysis, particularly in humans. While significant advances in imaging (Abdelfattah et al. 2019; Yildirim et al. 2019) and microelectrode array technology have made exploring neural activity at the microscale level increasingly accessible (Jia et al. 2019), activity types beyond single-cell extracellular spikes and LFP oscillations have not been studied in vivo in humans.

We took advantage of newly developed high-density poly(3,4-ethylenedioxythiophene) polystyrene sulfonate (PEDOT:PSS) microelectrodes to detect microscale neural activity from large areas of the cortical surface in humans, rodents, and nonhuman primates (Wilks et al. 2011; Sessolo et al. 2013; Khodagholy et al. 2015, 2016, 2017; Cellot et al. 2016; Hermiz et al. 2020). PEDOT:PSS microelectrodes represent a next stage in technologies developed for recording microscale neuronal activity in humans. A significant advantage of the PEDOT:PSS microelectrode grids is that they can lay over the top of the cortex without penetrating the pial surface, covering large areas of the brain (Wilks et al. 2011; Sessolo et al. 2013; Khodagholy et al. 2015, 2016, 2017; Cellot et al. 2016; Hermiz et al. 2020). These arrays can be fabricated easily, conform to the surface better than other surface array types (e.g., silastic), and can be customized for a wide range of configurations (Wilks et al. 2011; Sessolo et al. 2013; Khodagholy et al. 2015, 2016, 2017; Cellot et al. 2016; Hermiz et al. 2020). Their properties and recordings can be compared with other microelectrode systems used in patients including laminar arrays of microelectrodes (Ulbert, Halgren, et al. 2001a; Ulbert, Karmos, et al. 2001b; Ulbert et al. 2004; Wang et al. 2005; Fabó et al. 2008; Cash et al. 2009; Keller et al. 2010; Halgren et al. 2018, 2019). Further microelectrode recordings can be done using 2D arrays of penetrating microelectrodes (the Utah array, Nordhausen et al. 1994; Hochberg et al. 2006; Schevon et al. 2008, 2010; Truccolo et al. 2008; Waziri et al. 2009; Keller et al. 2010). Importantly, specialized recording (including novel microelectrodes) and analytic approaches have been used to explore axonal action potentials (Robbins et al. 2013; Stuart and Spruston 2015; Jun et al. 2017), dendritic calcium spikes (Ross 2015; Suzuki and Larkum 2017; Golding et al. 2018), and backpropagating action potentials (Moore et al. 2017; Jia et al. 2019) in rodents. However, these events have not yet been systematically studied across multiple species, including humans, under multiple conditions.

We employed the high-density capabilities of PEDOT:PSS arrays and other microelectrode systems to detect and examine microscale cortical activity beyond action potentials and LFP oscillations in humans, rodents, and a nonhuman primate. More specifically, we used PEDOT:PSS microelectrodes to record patients undergoing craniotomies for surgical resection of tumor or epilepsy. We also analyzed recordings from semi-chronically placed laminar microelectrodes and Utah arrays. Our results included both LFP dynamics (typical of pial recordings with metal contacts; Kaiju et al. 2017) and high-frequency events similar to the single-unit activity seen in intraparencymal recordings with penetrating metal electrodes, which we label Type 1 events (Khodagholy et al. 2015, 2016). Remarkably, we noted two other classes of morphologically, spatially, and temporally distinct events with features between single-unit activity and slower oscillatory events; we call these Type 2 and

Type 3 events. To demonstrate these events are not artifacts, we examined their presence and characteristics across multiple microelectrode types, species, and experimental conditions, and we concluded that these events physiologically originate in brain activity and are distinct from ongoing spontaneous oscillations.

Materials and Methods

We characterized neural activity as recorded with surface high-density poly(3,4-ethylenedioxythiophene) polystyrene sulfonate (PEDOT:PSS) microelectrodes in four different centers; across 37 patients, in four mice, and a nonhuman primate (NHP); and with two different recording systems. We also examined neural activity recorded via Utah array microelectrodes and laminar microelectrodes and via single-channel sharp electrodes recorded during deep brain stimulator (DBS) surgery (Patel et al. 2013; Jamali et al. 2019). Here, we first describe PEDOT:PSS electrode manufacturing and configurations, followed by acute electrode placement procedures for the operating room (OR). We then explain implantation and recording from the laminar and Utah array semi-chronic implants in humans as well as procedures for defining the mouse and NHP recordings. We also include details on the different tests we performed in the OR. Finally, we recount data analysis methodologies.

PEDOT:PSS Electrode Device Fabrication

The PEDOT:PSS device was fabricated similarly to previously established protocols with slight modifications as noted below (Uguz et al. 2016; Ganji, Atsunori, et al. 2017a; Ganji, Kaestner, et al. 2017b). Si wafers in batches of six were used as substrate carriers to deposit parylene C layers. Following substrate cleaning, the diluted Micro-90 (0.1%)—an antiadhesion layer—was spun-cast at 1300 rpm on the substrate and an NR9-6000PY negative resist was used for metal electrode definition on the parylene C layers. O_2 plasma (Plasma Etch PE100) was applied for 2 min (150 W RF power, 5 sccm O_2) as a descum step to remove residual photoresist in patterned regions prior to the evaporation of a 15-nm Cr adhesion layer and a 100-nm Au contact layer on top of the 4-μm-thick parylene C layer (epidural mouse recording) or 10-μm-thick parylene C layer (subdural recordings for mouse, NHP, and humans). After lift-off, an O_2 plasma (Plasma Etch PE100) was applied for 2 min (150 W RF power, 5 sccm O_2) to activate the parylene C surface to enhance the adhesion of the subsequent 2-μm-thick encapsulating parylene C layer. Another higher concentrated Micro-90 (1% as opposed to 0.1% for the first layer) layer was spun-cast and a third parylene C layer (≈1.9–2.5 μm) was deposited as a sacrificial layer. To define the patterns on electrode sites, a 10-μm-thick 2010 SU-8 photoresist layer was exposed and developed using Karl Suss MA6 mask aligner and SU-8 developer. Prior to PEDOT:PSS deposition, O_2 plasma (Oxford Plasmalab 80, 200 W RF power, 32 min) was used to etch the openings in the third and second parylene C layers all the way to the contact sites. Additionally, a hole at the center of the circular array was etched through all parylene C layers. The remainder of the fabrication process was essentially as previously reported (Rivnay et al. 2016; Uguz et al. 2016; Ganji, Kaestner, et al. 2017b), though we have several recommendations to improve quality control and yield successful recordings. First, we observed that using thicker (14 μm) parylene C layers, noted above for subdural recording in mice, NHPs, and humans, resulted in additional mechanical stability that improved device yield throughout postfabrication evaluation, packaging, shipping, sterilization, and use in the OR. Second, we used graded widths of parylene C from the connector region to the microcontact region to distribute stresses more evenly and avoid 90° cuts or patterns in parylene C, which can nucleate cracks and tears under stress. Third, we found that incorporating perfusion holes through the grid can improve conformal contact between the grid and the brain surface, which in turn resulted in higher fidelity recordings. At last, we noted that functional channels on the brain surface had higher yield when the operating neurosurgeon had more experience using the device. Carrying out mock-placement experiments using these and other similar grids might help raise the success rate and yield of the OR recordings.

We used four different PEDOT:PSS electrode designs. One electrode type involved two columns of 64-channel 20-μm diameter contact sites with 50-μm center-to-center pitch between adjacent contacts, which we call the 50-μm pitch 2-column grid ($N = 25$; Fig. 1; Supplementary Figs 1, 2 and 4). A second array had the same material make-up but the center-to-center pitch was 800 μm; we call this the 800-μm pitch 2-column grid ($N = 1$; Supplementary Figs 3, 5). A third array was a 128-channel grid with concentric rings at varying distances between each electrode site, which we call the circular grid ~4 mm in diameter ($N = 11$; Supplementary Figs 3, 5). One array, used while recording over the mouse barrel cortex, was a square grid of 32 channels.

Ethics Statement

All patients voluntarily participated after fully informed consent according to NIH guidelines and as monitored by the Partners (currently Massachusetts General Brigham) Institutional Review Board (IRB), which provides coverage for Massachusetts General Hospital (MGH), Brigham and Women's Hospital (BWH), and Boston Children's Hospital; by the UC San Diego Health IRB, which provides coverage for the University of California San Diego (UCSD), the New York University Medical Center IRB for New York University Medical Center, Committee on Clinical Investigations of the Beth Israel Deaconess Medical Center for Beth Israel Deaconess Medical Center, the Hungarian Medical Scientific Council, and the Oregon Health Sciences University IRB for the Oregon Health Sciences University (OHSU). Participants, whether being recorded in the OR or with semi-chronic electrodes in the epilepsy monitoring unit, were informed that participation in the experiment would not alter their clinical treatment in any way and that they could withdraw at any time without jeopardizing their clinical care.

Human Participant Recordings in the OR

Recordings of humans in the OR were acquired from 37 participants (mean = 39.7 years old, ranging from 22 to 62; 18 women; all but 7 individuals right-handed Supplementary Tables 1 and 2) who were scheduled for surgical resection of cortical tissue, as a result of tumor or epilepsy, at MGH, BWH, UCSD, or OHSU. Patients were already scheduled for a craniotomy for concurrent clinical intraoperative neurophysiological monitoring; testing to map motor, language, and sensory regions; or tissue removal.

In some cases ($N = 9$), participants received pro-convulsant medications (methohexital or alfentanil) intravenously while undergoing clinical mapping of the putative seizure focus as well as recording with the clinical electrodes. This choice was made

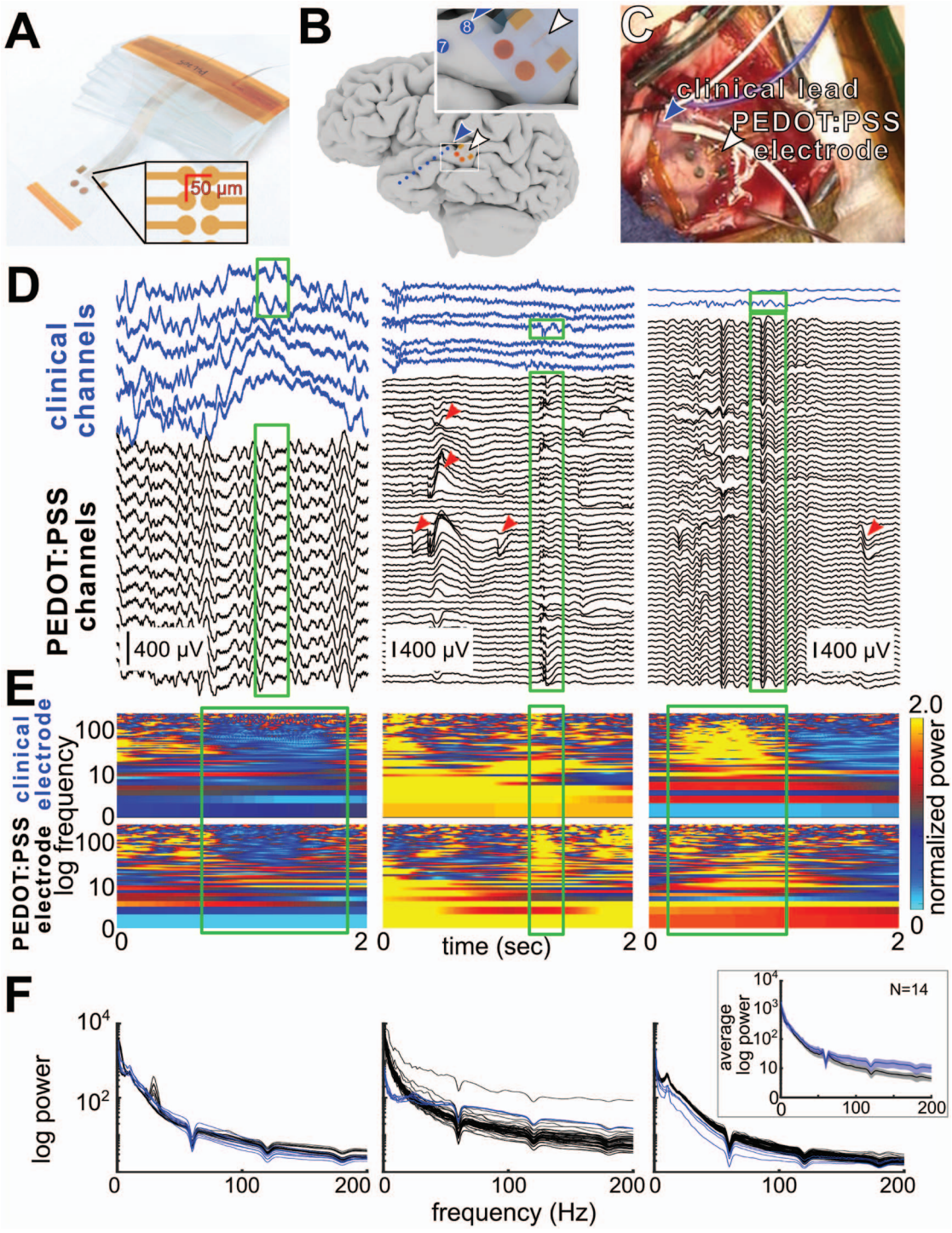

Figure 1. PEDOT:PSS recording setup, fast events, and spectrum. (*A*) PEDOT:PSS 2-column 128-channel grid electrode layout (two rows of 64 channels separated by 50 µm) and dimensions. (*B*) Example of relative positioning. The larger orange circles and squares on the electrode array indicate large PEDOT contacts to orient the small electrode contacts (the 2-column grid, white arrowhead) between the two large squares. The adjacent clinical electrode is seen in blue (with blue arrowhead). The inset square is a zoomed-in view of the PEDOT:PSS electrode. (*C*) Photograph of microelectrode (white arrowhead) and clinical array (blue arrowhead) on the human cortical surface alongside reference electrodes (white and purple wires). (*D*) Example broadband recordings, from three participants (IP03, IP15, and IP18), of clinical leads (blue lines) and the PEDOT:PSS grid (black lines, bottom), with unitary events (red arrowheads, grid middle, and right traces). The geometry of the PEDOT:PSS grid in all three recordings was a 128-channel 2-column grid extending 3150 µm × 50 µm with a 50-µm pitch between sites. The time scale traces in *D* and *E* are the same. (*E*) Normalized power spectrograms of the simultaneous individual clinical and PEDOT:PSS recordings and one same-channel trace shown in *D*. Normalization was done by dividing each time step in power per frequency band by the mean power across all time windows per frequency band. Each LFP column traces in *D* match the spectrograms shown in *E*. (*F*) Individual average power spectra curves for PEDOT:PSS (black) and clinical (blue) channels for IP03, IP15, and IP18. Inset: Average values across participants ($N = 14$). Green boxes in *D* and *E* highlight similar dynamics between the clinical (top row in *D* and *E* separately) and PEDOT:PSS recordings (bottom row in *D* and *E* separately). Shaded regions indicate SEM.

by the clinical team. For another subset of cases ($N = 8$), cold saline was applied to either clinically reduce tissue overactivity or determine how a change in temperature alters underlying activity. Finally, repetitive sounds including real words, nonsense syllables that were not English words, and noise-vocoded white noise convolutions of real words (1 s between each sound) (Travis et al. 2013; Hermiz et al. 2018; Kaestner 2018) were played back to some participants ($N = 11$) via either a speaker in the OR ($N = 4$) or headphones worn by the participant ($N = 7$) using Presentation software (Neurobehavioral Systems) to determine auditory response.

Following surgery, the preoperative T_1-weighted MRI was reconstructed using FreeSurfer scripts (Reuter et al. 2010, 2012; Dykstra et al. 2012) (http://surfer.nmr.mgh.harvard.edu). Using blender software (https://www.blender.org/) and MMVT, the reconstructions were then aligned to images obtained during surgery (Holmes et al. 1998; Dykstra et al. 2012; Felsenstein and Peled 2017; Peled et al. 2017). The method involved projecting the surgical image onto the patient's reconstructed brain using blender and then placing a 3D model of the PEDOT:PSS electrode array on that location, similar to other coregistration approaches (Holmes et al. 1998; Postelnicu et al. 2009; Dykstra et al. 2012) (Fig. 1; Supplementary Figs 1–3).

In addition to the participants mentioned above, we examined data from two additional patients who underwent intraoperative neurophysiology as part of their planned DBS placement (Patel et al. 2013; Jamali et al. 2019). These types of recordings are detailed in previous studies (Patel et al. 2013; Jamali et al. 2019). As with the PEDOT:PSS recordings, patients were informed that they could withdraw from the study at any point without altering their clinical care. Because patients receiving DBS implantations at MGH normally also undergo standardized microelectrode recording to optimize anatomical targeting (Amirnovin et al. 2006; Patel et al. 2013), microelectrodes can traverse the dorsal lateral surface of the prefrontal cortex on the way to the target nucleus, offering a brief chance to study neuronal dynamics in the dorsolateral prefrontal cortex (dlPFC). Importantly, these recordings neither perturb the planned operative approach nor alter clinical care (Sheth et al. 2012; Patel et al. 2013; Mian et al. 2014). The three microelectrodes (500–1500 kΩ) (Alpha Omega Engineering) were moved simultaneously at 10–100 µm increments to identify and isolate individual units in the cortex. Once unit-like spikes were observed in the recording, the micro-electrodes were maintained in position for 4–5 min to confirm signal stability. The signal was sampled at 44 kHz, then decimated to 1000 Hz. The same analyses as described below for event detection, and dynamics were then applied.

Semi-Chronic Human Participant Recordings in the Epilepsy Monitoring Unit

Patients with pharmacologically resistant epilepsy who were undergoing surgery to locate and resect seizure foci received laminar and Utah array electrode implantation (Supplementary Table 3). All decisions concerning placement were made with clinical input, particularly since both the Utah arrays and laminar microelectrodes were inserted into cortex likely to be resected. Laminar recordings were made in the United States of America and Hungary, while the Utah array recordings were performed in the United States of America. Both array types are placed in the cortex and are generally under a grid of clinical macroelectrodes. Insertion into the pial surface and pressure from the brain relative to the grid or dura over the brain helped keep the microelectrodes in place. In addition, the clinical grid further secures them to prevent movement. The electrodes were implanted for a period of several days to 2 weeks. We analyzed recordings from periods of quiet wakefulness separated by at least an hour from seizure activity.

Nine patients (mean = 23.375 years old, ranging from 12 to 42; 4 women) received laminar electrodes. Laminar microelectrodes were implanted perpendicular to the cortex in noneloquent tissue that was ultimately resected, has been reported on previously (Ulbert, Halgren, et al. 2001a), and used in a number of studies (Ulbert, Karmos, et al. 2001b; Ulbert et al. 2004; Wang et al. 2005; Fabó et al. 2008; Cash et al. 2009; Keller et al. 2010; Halgren et al. 2018, 2019). Each laminar probe spanned the cortical depth with a length of 3.5 mm and a diameter of 0.35 mm. The laminar probes are 3.6-mm-long, 350-µm-wide tubular shafts made of polyimide which is flexible but sufficiently stiff to penetrate the cortex without additional mechanical support. A silastic "cap" resting on the pial surface keeps the laminar arrays in place and helps maintain probe position. Each array is a single laminar column containing 24 electrodes with diameters of 40 µm and a center-to-center pitch of 175 µm. Neural data were recorded and stored continuously at a rate of 2 kHz in the EEG range simultaneously with multiunit activity (MUA) range activity sampled at 20 kHz. Please see prior publications for methodological details.

Another eight patients (mean = 32 years old, ranging from 21 to 47; 2 women) were implanted with Utah array (also called NeuroPort array) electrodes (Blackrock Microsystems), which have been used in several previous studies (Hochberg et al. 2006; Truccolo et al. 2008; Waziri et al. 2009; Schevon et al. 2010). The 4 mm × 4 mm microelectrode array is composed of 100 platinum-tipped silicon probes at two different depths. In four cases, the electrodes penetrated 1.0 mm into the cortex, 1.5 mm in the other four cases.

NHP Surgical Details and Recording Methods

Intraoperative, intracranial neurophysiology recordings were acquired from one adult male rhesus macaque (*Macaca mulatta*, age 14; Supplementary Table 4) according to the Guide to the Care and Use of Laboratory Animals. All efforts were made to minimize discomfort, and the Institutional Animal Care and Use Committee at the Massachusetts General Hospital monitored care and approved all procedures. The macaque was placed under general endotracheal anesthesia (isoflurane) and placed into a stereotactic frame (Kopf). A craniotomy over the visual cortex was performed using standard anatomic landmarks, and cortex was carefully exposed. Using gyral anatomy and vasculature over V1 versus V4, the V4 area was identified visually and a PEDOT:PSS electrode was placed over the region. Signals were recorded using the ORH128 Intan Recording System (Hermiz et al. 2016, 2018). Data were acquired at 30 kHz and filtered by the default Intan setting, with cutoffs 1–7.5 kHz, and using OpenEphys acquisition graphic-user interface software (Siegle et al. 2017) (http://www.open-ephys.org/). Electrode impedance testing during the experiments employed the Intan RHD2000 software from Intan Technologies. Data were extracted and processed using MATLAB (Mathworks).

Area V1 Mouse Surgical Details and Recording Methods

The care and use of mice (2–6 months old; C57BL/6J; Jackson Laboratory; Supplementary Table 4) followed all federal and institutional guidelines, and the Institutional Animal Care and Use

Committees of the Massachusetts General Hospital approved all procedures. Mice were deeply anesthetized with a cocktail of injected ketamine hydrochloride (100-mg/kg intraperitoneal injection) and xylazine (10-mg/kg i.p. injection; $N = 1$) or isoflurane administered as a gas prior to and at the start of surgery ($N = 2$). In the mouse given ketamine, additional ketamine (1/10 initial dose) was supplemented every 30 min to maintain the plane of anesthesia.

Anesthetized mice were placed into a stereotaxic frame (Narishige) for the craniotomy as well as all subsequent testing. A heating blanket on the frame floor maintained body temperature at 37 °C. A craniotomy was performed on a 4.5 mm × 4.5 mm area around the primary visual cortex (V1) defined by a stereotaxic coordinate (AP: −3.8, ML: −2 mm; Paxinos and Franklin 2001). After the cranium was removed, the PEDOT:PSS array was placed over the exposed visual cortex over intact dura. Once the PEDOT:PSS array was positioned on V1, neural signals were recorded using the ORH128 Intan Recording System, acquiring data at 30 KHz, and filtered by the default Intan setting (cutoffs 1−7.5 kHz). Data were extracted and processed using MATLAB.

Barrel Cortex (S1) Mouse Surgical Details and Recording Methods

All procedures were in accordance with a protocol approved by the Institutional Animal Care and Use Committees of UC San Diego (Supplementary Table 4). ICR mice weighing 25–35 g were anesthetized with isoflurane; a femoral artery was catheterized to allow recording of blood pressure, and a tracheotomy was performed for ventilation. A metal headpost was fixed to the skull using dental acrylic, and a craniotomy and durotomy were performed over the right whisker barrel and surrounding cortex. The exposure was surrounded by a dental acrylic well in order to keep it filled with artificial CSF until the electrode array was placed. The exposure was dried prior to the electrode placement, and once the array was implanted, it was covered with 0.7% agarose in artificial CSF. The PEDOT:PSS electrodes arrays had contacts arranged in square grids with 0.2 mm spacing between 50-µm-diameter contacts. The reference electrode was a silver-chloride ball placed between muscle tissue exposed for the craniotomy. Prior to recording, the mice were administered pancuronium and artificially ventilated, and prior to stimulus trials, the mice were switched from isoflurane to alpha-chloralose anesthesia. Whisker flick stimuli were presented every 2 s through analyses, and event detections were taken at baseline and during nonstimulated periods of time. Neural signals were recorded at 20 kHz using the Intan recording system.

Data Acquisition: Acute Intraoperative Recordings

Most human intracranial recordings, taken in the OR from the PEDOT:PSS electrodes, were made using a custom Intan recording system with a sampling rate of either 20 or 30 kHz (filtered from 1 to 7500 Hz to reduce aliasing; Intan Corporation). During acquisition, recordings were referenced to sterile ground and recording reference needle electrodes (Medtronic) placed in nearby muscle tissue or scalp, as deemed safe by the neurosurgeon. After the electrode array was laid on tissue and the grounds placed, we tested impedances using the Intan system employing the RHD2000 series software (Intan Corp.). In most cases, we used OpenEphys (Siegle et al. 2017), an open-source software which allowed us to save and visualize activity across all 128 channels as well as the analog input. Trigger signals produced by a custom MATLAB program indicating the hour, minute, and second were additionally sent to both the analog input for the Intan system and the TRIG input for the clinical Quantum system (Natus) which acquired the concurrent clinical electrode recordings. The clinical Quantum system recorded neural activity at either 4096 Hz (at MGH) or 512 Hz (at BWH). At UCSD and OHSU, we recorded neural activity using the PEDOT:PSS electrode only. To test whether activity we observed was due to the Intan system, we also recorded neural PEDOT:PSS activity using a second recording system with a sampling rate of 30 kHz, a high-impedance headstage, and amplifiers input to a Neural Signal Processor (Blackrock Microsystems). In one case, two PEDOT:PSS electrodes, one connected to the Intan system and the other to the Blackrock system, were used to record simultaneously as a side-by-side comparison (Supplementary Fig. 3).

Data Acquisition: Semi-Chronic Laminar and Utah Array Recordings

For the laminar recordings, differential recordings were made from each pair of successive contacts. After wideband filtering (DC—10 kHz), the signal was split into a low-frequency field potential band (filtered at 0.2–500 Hz, gain ×1000, digitized at 2 kHz, 16 bit) and stored continuously. Periods of time where there were clear artifacts were rejected from the laminar recordings.

Utah array recordings were made from 96 active electrodes and data were sampled at 30 kHz per electrode (0.3–7 kHz bandwidth) using Blackrock hardware. Recording data from the Utah arrays were taken from 30 min of baseline activity while participants were awake (around 11 am) 3–4 days after implant. These baseline recordings were made while participants were awake and engaged (as checked via simultaneously recorded video). This data selection was done to ensure consistency between data sets.

Saline Recordings

For a subset of cases ($N = 6$), in the OR, we took several minutes of room temperature saline bath recordings minutes before or after recording from the brain, using the same equipment and electrodes as in neural tissue recordings. For all comparisons, we conducted the same analyses and classification steps, as listed below, on these saline tests to determine if we could observe the same events identified in the brain OR recordings. In two cases, we purposefully shifted the electrode in the saline to reproduce movements.

Electrical Stimulation

Electrical stimulation occurred in $N = 11$ cases (Supplementary Table 1). For most of these, neural stimulation had clinical purposes, such as evaluating motor or language mapping (Mueller and Morris 1993; Borchers et al. 2012). Stimulation used either a Prass Standard Monopolar Stimulating Probe (motor mapping cases), Disposable Double Ball Tip Nerve Stimulating Probe (speech mapping cases), or the Nicolet Cortical Stimulator for Neurosurgery (Natus Neurology Inc.). For clinical stimulation mapping ($N = 9$), trains (at 60 Hz) or pulses of variable length (ranging from 0.1 to 1 s) and amplitude (ranging from 1 to 10 mA) were delivered via a hand-held bipolar wand at different locations personalized to surgical flow. Research stimulation ($N = 2$)

consisted of train stimulation (100 Hz, 0.5-sduration) delivered at 5-s intervals via a pair of surface clinical strip electrodes near the PEDOT:PSS electrode.

Intraoperative Video Monitoring

With the patient's informed consent, surgeries were video recorded by a camera set in the OR light (Black Diamond Video). We approximated video recording timing by annotating when the electrode was placed on and removed from the brain, actions that could also be seen in the recordings. We also noted the timing and location of stimulation via bipolar contacts or PEDOT:PSS electrode movements to confirm the timing of noisy signals relative to additional experimental events. Additionally, photographs were taken to illustrate electrode location (Fig. 1).

Data Analysis

Data analysis was performed using custom MATLAB programs. Cross-correlation between resampled analog trigger signals was used to align the triggers between multiple systems, both between the neural data and between the audio recordings. Since the recordings were brief (4–20 min) and electrodes could be moved at any point, we used the video and audio recordings as well as the voltage recordings to determine stable recording periods.

"Raw" voltage signals were taken directly from the Intan recordings. LFP data were decimated to 1000 Hz and demeaned relative to the entire recording. MUA or spike-related activity were detected by high-pass filtering the signal above 250 Hz. Channels with excessive line noise, high impedances ($>100\ k\Omega$), or fluctuations across the voltage range were removed from the analysis. We also noted that, since these OR recordings are necessarily transient, over time some channels became noisier than others during the recordings. For this reason, we conducted root mean square (RMS) calculations of electrodes for the "quiet" periods when the electrode was not being moved and there were no visible inter-ictal discharges (IIDs) or stimulation (Supplementary Fig. 6). We found that, by and large, the recordings in channels that had within-range impedances also had low RMS values (around or below an RMS of 5). However, a subset of channels had high RMS values (closer to an RMS of 20–50); we excluded these from further analyses. These channels tended to have recordings that were unstable over time due to fluctuations in voltage and the presence of 60-Hz noise. After excluding the recordings from one participant, $48.5 \pm 23.26\%$ of the electrode contacts (channels) survived channel rejection criteria across patients (Supplementary Table 2; Supplementary Fig. 6; see Materials and Methods). As we progressed in cases and gained experience, the percentage of good electrode contacts improved, reaching closer to 80%. We also found that channels, which survived the rejection criteria, varied considerably in terms of location across the grids (Supplementary Figs 4 and 5) and that these productive locations did not correspond to amplifier bank or physical connectivity (e.g., particular cables or connectors).

Type 1 Sorting

We first sorted Type 1 waveforms from the data that were high-pass filtered above 250 Hz using a Butterworth filter via Offline Sorter (v4, Plexon, Inc.). We identified unit waveforms as activity within the range of 15–500 µV and with a duration between 500 and 1500 µs. However, the pitch and high density of the electrodes generated too many "units" since the putative units spanned multiple channels in the recording. For this reason, we used the newest Kilosort2 (Pachitariu et al. 2016), which omits spike detection and PCA and instead combines template waveforms, associated spike locations, and spike times into one model to arrive at potential units. The mean waveforms for these "neurons" are swept repeatedly through the voltage data as a template, and the newly detected spikes that match these templates are subtracted away, leaving behind the residual data which can be iterated through again. The software also considers electrode spatial arrangement, allowing sorting on high-density electrodes such as Neuropixel (Jun et al. 2017; Jia et al. 2019). As such, we included a specific channel map for each array. These data were processed with default Kilosort2 parameters for configuration (code located at https://github.com/Center-For-Neurotechnology/LFP-Type2-and-Type3-Detection) except that the acceptable firing rate for a unit was allowed to go below 0.1 Hz. This expansion increased sensitivity to units that might fire very infrequently over the short recording period. Additionally, our threshold for Kilosort spike detection was (as a default) –6 standard deviations (SD).

Before processing, we only applied Kilosort2 to data with no movement or stimulation artifact, and we removed noisy channels. Putative event clusters (equalivalent to single units) were rejected if the captured waveforms seemed to be artifacts (as with stimulation) or if the units had highly regular or too short interevent intervals. Rejecting events with inter-event intervals (IEIs) that either corresponded with 60 Hz noise or occurred at the same time as the stimulation, we identified the fast waveforms in the raw and original high-pass filtered data to confirm their timing and channel location. Because the event count was low, we attempted to merge clusters based on spatial mapping of the recordings. However, merging clusters produced significantly more violations of the 2–5 ms minimum refractory period, meaning that the merged clusters were more likely to be MUA, thereby indicating that these events must be separated to more similarly represent single-unit activity. Therefore, we did not merge clusters, nor did we autocorrelate event times to make any decisions to merge clusters. This approach aligns with preliminary findings about the similarity between manual and automatic spike sorting (Steinmetz et al. 2020). In other words, results produced by manual sorting, which often involves more per-analyst variability, are similar to those generated by Kilosort; the only difference is that Kilosort2 can be more automatic and possibly more replicable across instances using the same configuration file. Of note, we could not easily use signal-to-noise ratio (SNR) as a method to test cluster quality, as SNR usually assumes event detection on one or a few channels. In contrast, we use Kilosort2 to identify event clusters with high spatial resolution across 7–10 channels on the PEDOT:PSS grid where spatial and waveform characteristics define each cluster across the spatial map. This approach can lead to large waveforms on some channels and no waveforms on others (Fig. 2). Therefore, SNR, and SNR variance, may not be as informative as other recording approaches.

Type 2 and 3 Event Detection and Template Matching

Since other "events" involved both short (Type 1) and long (traveling LFP wave) timescales and varied in size and direction of deflection (due to changes in voltage polarity across electrodes), we performed a first-pass visualization to detect and annotate

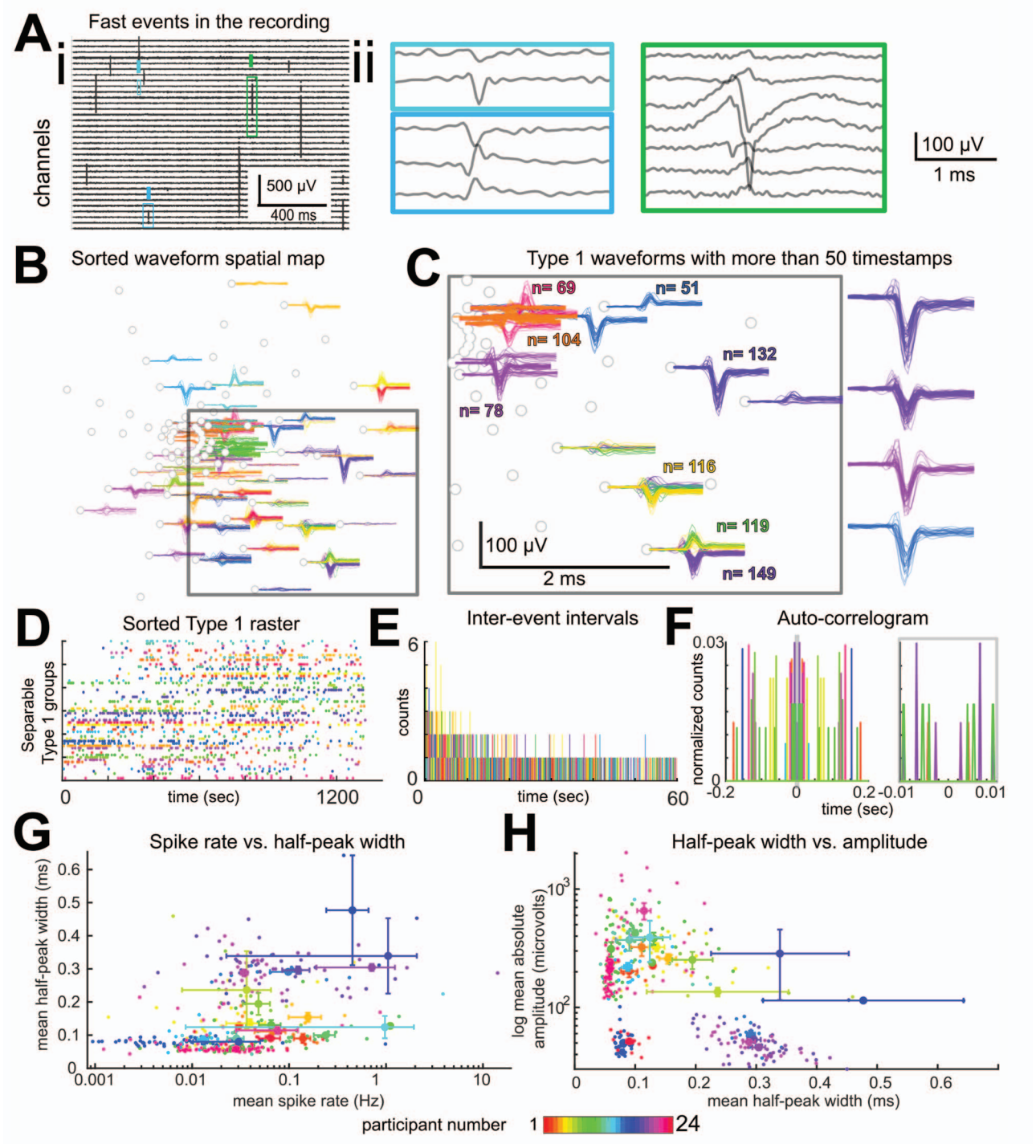

Figure 2. Fast Type 1 events recorded from the surface of the human cortex. (*A*, i–iii) Example recording from participant IP37. In ii, the events in colored boxes from i are shown at higher resolution. (*B*, *C*) Example fast waveforms from the same participant, mapped to the circular grid locations across the PEDOT:PSS microelectrode array. The waveforms are color-coded to correspond to different clusters as determined in Kilosort using waveforms' spatial locations on the PEDOT:PSS grids combined with spike times in a model (see Materials and Methods). The gray dots indicate good channels with low impedance on the circular PEDOT:PSS array. (*D*–*F*) Example recordings from the same clusters as in *B* and *C* shown as a raster plot across the microelectrode grid, as IEIs (*E*), and as auto-correlograms (*F*) for a subset of clusters with different time scales at ±0.2 s (left plot) and ±0.01 s (right plot). (*G*, *H*). Comparisons of half-peak widths versus event frequencies (spike rate; *H*) and half-peak widths versus trough-to-peak amplitudes (*G*) of the sorted waveforms across all participants. $N = 24$. Error bars indicate SEM.

electrode movement, stimulation, and the presence of IIDs. For this process, we used Wonambi, a visualization tool originally used in sleep scoring (https://wonambi-python.github.io/). We rejected any time periods when the electrodes were being moved in the recording. For these analyses, we identified IIDs as events that were ~250-ms duration and similar to previously published IID waveforms (Curtis et al. 2012; Janca et al. 2015) but did not include those IID waveforms in the subsequent event classification analyses since we considered those events outside the scope of the current study.

Next, we detected peaks larger than 25 μV and took 400-ms snippets of data around each event (−100 to 300 ms) per channel. We then realigned events relative to the largest rising or falling edge (for easier comparisons across waveforms). After examining all waveforms both singly and using PCA (Supplementary Fig. 8), we found that we could further remove noise through template matching to the latter two of three main waveform types: 1) Type 1: fast repeated waveform events, detected between 250 and 6000 Hz; 2) Type 2: peaks with sharp rise and slow fall, ~10–30 ms absolute half-peak duration, detected below 500 Hz; or 3) Type 3: peaks with slow rise and slow fall, ~100 ms absolute half-peak duration, detected below 500 Hz. Templates were constructed from average identified waveforms across the dataset, based on the event rates and most common waveforms identified through PCA, which included the Type 2 and 3 events (Supplementary Fig. 9). Since we were template matching the LFP, not the raw data, we would not be able to detect Type 1 events using this approach. The template matching was done by correlating each detected waveform with the template waveforms and only including waveforms and time points with correlations to Type 2 or Type 3 events above 0.8. These detections were used to exclusively bin each event into one of these two types.

One possible explanation for these events is that they result from electrical noise or some kind of mechanical artifact. To address this, we examined saline recordings taken in the OR using the same electrodes for several minutes before and after recording from the brain in $N = 6$ cases (Supplementary Figs 10–12). In two cases, we moved the saline bowl in an attempt to reproduce the waveforms observed in the neural recordings. First, the Type 1 events observed in the neural recordings were not present in any of the saline recordings (data not shown). We either never or very rarely detected Type 2 events in any of the saline recordings, with or without movement (Supplementary Figs 10–12). When we moved the electrode in the saline, waveforms similar to the Type 3 events could be identified in the saline recordings, although these were rare compared with findings in the neural recordings. Furthermore, the waveforms were visibly slower to rise and fall, resulting in a lower second derivative of the onset time (Supplementary Fig. 10) without the sharp initial rise of Type 3 waveforms observed in the neural recordings, meaning that brain-recorded Type 3 waveforms had higher second derivatives around the waveform onset (Supplementary Figs 10–12). After examining the saline recording detections and finding overlap between waveform types in the brain and saline recordings, we added, as another detection step, thresholding based on the second derivative at ±50 ms around the waveform onset (Supplementary Figs 10–12). Finally, to remove the possibility of including ongoing oscillatory waveforms, we added a final, fourth step to retain only waveforms with average absolute voltages less than 25 μV in the preceding 100 ms before event onset.

Even after these added waveform onset thresholding steps, most Type 2 and 3 events recorded on the brain surface survived the thresholding per participant (Supplementary Fig. 10). We found that both event types happened significantly more frequently on brain tissue than in saline ($P = 0.0038$; Kruskal–Wallis multiple comparison test; Supplementary Fig. 12), with sum totals of 59 Type 2 events and 854 Type 3 events across nine saline recordings over 29 min versus 3553 Type 2 events and 33608 Type 3 events on brain tissue using the same electrodes over the same amount of time. Additionally, using our spatial extent detection window over a total period of 29 min, we found that 90% of events in saline spanned a single channel, with only six Type 2 events and 77 Type 3 events spanning multiple channels (Supplementary Fig. 12).

The Type 2 and 3 LFP events were then mapped to the recordings by time to determine if their rates, sizes, and temporal dynamics vary with the introduction of auditory stimuli, proconvulsant medication, cold saline, or electrical stimulation. We quantified these categories' rates in time as IEIs and the absolute amplitudes of the voltage deflections from baseline. We examined the rise and fall times relative to the peaks by quantifying the RC time constants $\tau_{\text{rise time}}$ and $\tau_{\text{fall time}}$ as in the following equation: $\Delta V = (V_{\text{final}} - V_{\text{start}})*(1 - 1/e\text{^}(\text{time}/\tau))$, where $\tau_{\text{rise time}}$ was calculated as the time required for the voltage to reach 0.63 of the maximum peak and $\tau_{\text{fall time}}$ was calculated as the time required for the voltage to reach 0.37 of the fall back to baseline.

Additional measures included evaluating events' temporal and spatial spread in a recording with identifying events that were concurrent in time, that is, within 5 ms of each other, across channels and calculating their spatial spread based on the electrode layout. Peri-stimulus time histograms (PSTHs) binned activity in time around specific treatments, such as proconvulsant medications, cold saline, auditory stimulation, or electrical stimulation. The bins were one at 100 ms or at other time points depending on the treatment. PSTHs and IEI counts were normalized relative to baseline by dividing each bin by the average bins during the baseline recordings before averaging PSTHs across participants. Cross-covariance measures were calculated by converting the timing of the Type 1, Type 2, and Type 3 events in into 1-ms bins throughout the recording (at a sample rate of 1000 Hz) and then performing a cross-covariance between the event types. Autocorrelograms used a leave-out method that involved cross-correlating the timestamp of each treatment in a recording with all other events in that Type 1 group or per channel for the Type 2 and 3 events. This resulted in a lack of a peak at time = 0 with rhythmicity patterns emerging if there are periodic elements.

Spectral Analyses

Power spectral analyses to compare the simultaneous clinical and PEDOT:PSS recordings were performed using 5-min "quiet" periods (without movement, stimulation, or tasks and before application of medication or cold saline), taking the real value of the Morlet wavelet coefficient (power) at a 1-Hz spectral resolution using a moving window of 0.5 s moving every 10 ms, calculated using the Fieldtrip toolbox (www.ru.nl/fcdonders/fieldtrip). This approach allowed us to observe dynamics through time and as an average.

Event-triggered spectral analyses included the 30 s around each event (Type 1, 2, and 3) sampled at 1000 Hz and recalculated power with the real value of the Morlet wavelet coefficient

(power) at a 1-Hz spectral resolution using a moving window of 0.5 s moving every 10 ms, calculated using the Fieldtrip toolbox (www.ru.nl/fcdonders/fieldtrip) (Oostenveld et al. 2011). We then normalized the power at each frequency band by dividing each time step in power per frequency band by the mean power across all windows of time per frequency band. Finally, we averaged the power per the following frequency bands: 0–4, 4–8, 8–15, 15–30, 30–55, and 65–200 Hz.

As the Type 2 and 3 events had sharp onsets and broadband effects on power, we clipped out 200 ms around each actual event. We then used two different spectral calculations to determine if the Type 2 and 3 events were part of an ongoing oscillation. One analysis involved a series of steps: 1) calculating spectrograms 10 s before and after Type 2 and 3 events (not including ±200 ms around each event); 2) performing the same calculation but adding or subtracting a time in the range of ±10 s (jittered time-locked power calculation) rather than centering around a Type 2 or 3 event; 3) evaluating the difference between the two spectrograms on a per-channel basis and averaging per patient; and 4) determining if that difference varies significantly from zero across the dataset.

To measure the phase relationships between the same-channel LFP and Type 2 and 3 event onset, we filtered the signal to each frequency band with eegfilt (EEGLab package; Delorme and Makeig 2004) and then calculated phase per frequency band (Hilbert transform) and averaged those phase values using the CircStats toolbox (Berens 2009). Because we performed these calculations on a per-channel and then per-case basis, we averaged phase values when the number of events per recording was greater than five, as phase is highly susceptible to low event counts.

Statistical Analysis

All statistical comparisons were performed using nonparametric measures, so we did not test for normality. We tested comparisons with the Kruskal–Wallis test for nonequivalence of multiple medians followed by the post hoc Tukey–Kramer method to determine statistically separable groups. For all comparisons, we first calculated the mean values per type of neural activity on the per-participant level and then compared the medians between conditions. Activity measurements were separated into baseline, during pharmacological manipulation, during stimulation (auditory or electrical), or during physiological manipulation. These divisions resulted in measurements taken from distinct samples for the manipulations aside from baseline activity, a period of time that was measured and compared multiply when needed in order to identify changes in activity. We used the Wilcoxon rank-sum test (two-sided) for comparisons between individual medians. We tested if values were significantly different from zero using the Wilcoxon signed rank test. We corrected by adjusting the target P-value (0.05) with a Bonferroni correction for the number of comparisons being done. For phase relationships, we performed the Rayleigh test for unipolar distributions (Berens 2009).

Data and Code Availability

Open source acquisition software OpenEphys (http://www.open-ephys.org/) and open source waveform sorting software Kilosort (https://github.com/cortex-lab/KiloSort) were used to record and analyze the neural data. Custom Matlab code (version R2019a), combined with open source code from the Fieldtrip toolbox (http://www.fieldtriptoolbox.org/), was used for the majority of the analyses and is available upon request.

Custom Matlab code for detecting Type 2 and 3 events is available on Github (https://github.com/Center-For-Neurotechnology/LFP-Type2-and-Type3-Detection). The code requires 1000-Hz neural data in microvolts as input and can be used to detect Type 2 and 3 events across recordings. Sample data are provided along with plotting examples showing the resulting detections. Further data that support the findings of this study are available from the corresponding author upon reasonable request.

Results

PEDOT:PSS Electrodes Record Neural Activity on the Surface of the Human Brain

We recorded neural activity on the cortical surface using PEDOT:PSS microelectrodes and clinical surface electrodes in patients undergoing craniotomy for either tumor removal ($N = 15$) or seizure focus resection for intractable epilepsy ($N = 22$). PEDOT:PSS electrodes are 30 µm in diameter and have a center-to-center pitch between 50 and 800 µm. We used four different electrode designs (including circular, 2-column, and square grid designs) to cover areas ranging from 0.1575 to 40 mm^2 (see Materials and Methods; Fig. 1A–C; Supplemental Figs 1–5). These different designs afforded different coverage over the cortex (Supplemental Figs 1–5). Fabricated on parylene C (5–14 µm thickness) into either 32- or 128-channel arrays (Supplementary Figs 2 and 3), electrodes were placed directly on and conformed to the pial surface of the exposed cortex. Recordings ranged from 4 to 25 min. With one participant (Intraoperative Participant 14, or IP14), the recordings were unstable due to electrode movement throughout the session and were therefore excluded from subsequent analyses. Once the electrodes were placed on the brain, we tested their impedance values. For electrodes and contacts that passed our criteria (which included within-range impedances and recording stability; see Materials and Methods, Supplementary Figs 4–6), average impedance values were 44.5 ± 26.0 (mean ± SD) kOhm.

We found the same widespread “normal” neural dynamics and spectral content in both the PEDOT:PSS recordings and the concurrent clinical electrode (3-mm-diameter platinum contact grids) recordings, which were aligned in voltage and spectral frequency dynamics (Fig. 1C–E). Recognizable events such as epileptiform IIDs occurred at the same time on the microelectrodes and clinical contacts, with similar spectral dynamics observed in the simultaneously analyzed spectrograms (Fig. 1D,E; note the green boxes; $N = 14$). To determine if the oscillations captured by the PEDOT:PSS electrodes were similar to those recorded by the clinical contacts, we calculated power spectral density for both recording modalities from 1 to 200 Hz for the same time windows in the aligned recordings (Fig. 1F; $N = 14$). Averaged power spectra through spontaneous activity recordings were not significantly different between the clinical contacts and the PEDOT:PSS recordings ($P > 0.07$ for comparisons at each frequency step; Wilcoxon rank-sum test; $N = 14$). We observed concurrent oscillations in both the PEDOT:PSS recordings and the clinical recordings. However, the PEDOT:PSS recordings showed notably localized stand-alone events which were not detected by the clinical contacts (red arrowheads in Fig. 1D; Supplementary Video 1).

PEDOT:PSS Electrodes Record Putative Spiking Activity from the Surface of the Human Brain

We detected a series of different "fast" waveforms in PEDOT:PSS electrode recordings filtered between 250 and 6000 Hz. Previous studies with these devices have recorded single action potentials from pial surfaces, including in humans (Wilks et al. 2011; Sessolo et al. 2013; Khodagholy et al. 2015, 2016, 2017; Cellot et al. 2016; Kaiju et al. 2017; Hermiz et al. 2020). Some of these events (which we call Type 1 events) had similar kinetics to single units (i.e., individual spikes) recorded with extracellular electrodes including prior surface PEDOT:PSS electrode recordings (Khodagholy et al. 2015, 2016, 2017; Fig. 2A). We used the Kilosort2 software package only to detect Type 1 events (Pachitariu et al. 2016) by sorting waveforms into separable repeated events using a template matching approach that considers waveform spatial spread across electrode sites, a process that identified clusters of repeated Type 1 events in 24 out of 36 participants (Fig. 2). We hypothesize that the presence or absence of Type 1 events was related to cortical surface contact (which can vary from case to case per clinical considerations and variable placement) as well as overlap on or near vessels or, in some cases, tumor tissue (see Supplementary Figs 1–3, Supplementary Tables 1 and 2, Fig. 1C). The average frequency (number of events in a time window) across participants was 0.13 ± 0.75 with a median of 0.026 Hz (Fig. 2C,D). IEI histograms and autocorrelograms showed diverse patterns both within a recording (Fig. 2E,F) and across recordings (Supplementary Fig. 7). We did not observe consistent rhythmicity for these Type 1 events.

The sorted waveforms were generally negatively deflecting, though each event could be seen as negative on some channels and positive on the others (Fig. 2), with voltage amplitudes of 123.3 ± 89.57 μV and a median of 93.2 μV (averaged per cluster and then averaged across participants, resulting in 18 513 detected events subdivided into 420 identified, sortable, replicable "units" detected across 24 participants, with 17.5 ± 16.8 clusters detected per participant; Fig. 2G,H). The half peak widths for the largest waveforms per cluster across the dataset averaged 0.49 ± 0.217 ms (Fig. 2B,C,G,H). While fast compared with most somatic action potentials, these values are within the waveform range established by previous recordings using sharp electrodes (e.g., Utah array) in the human cortex or in rodents and NHPs (Bartho et al. 2004; Keller et al. 2010; Vigneswaran et al. 2011; Robbins et al. 2013; Chan et al. 2014; Anastassiou et al. 2015; Hamilton et al. 2018; Trainito et al. 2019). However, some events had waveform kinetics that were faster or slower than anticipated and amplitudes that were larger than expected for neurons at the pial surface (Fig. 2B,C,G,H).

Slower Microscale Events Are Also Detectable on the Surface of the Human Brain

PEDOT:PSS electrode recordings also revealed microscale phenomena distinct from the fast waveform activity represented by Type 1 events (Figs 1 and 2; Supplementary Video 1). These discrete, slower events occurred across multiple channels in a single recording, varied in polarity across channels and in time, and could repeat through time across neighboring channels. Notably, these events could be separated into distinct classes based on duration, with some lasting 100–200 ms and others less than 20 ms. That such events were not restricted to a single amplifier chip or bank, cable, recording system, or other physical structure indicates that they likely have physiological origins (see Materials and Methods). Having observed these waveforms repeatedly across participants and recordings, we set out to classify and characterize the corresponding waveforms to determine whether these events were spatially and temporally discrete, were part of ongoing oscillations, could be modulated, or had a significant relationship either to the detected fast waveforms or to each other.

To probe these waveforms, in addition to Type 1 (fast 1–2 ms duration events, detected in recordings filtered between 250 and 6000 Hz; Fig. 1), we defined two other events types: Type 2 events with a sharp rise and slow fall, ~10–30 ms absolute half-peak duration, detected in recordings filtered below 500 Hz and Type 3 events with a slow rise and slow fall, ~100 ms absolute half-peak duration, detected in recordings filtered below 500 Hz (Fig. 3A–E; Supplementary Video 1). We wondered whether these events were simply IIDs (Curtis et al. 2012). To further explore this possibility, we combined an automatic IID detection algorithm (Janca et al. 2015) with a visual check by an experienced electroencephalographer (see Materials and Methods). The detected IIDs were most often separate from the Type 2 and 3 events and usually spanned the entire electrode array, while Type 2 and 3 events were localized on the grids (Fig. 3E).

Initial Type 2 and 3 waveform classifications, even relative to IIDs, were based on visual inspection and spectral analysis. However, as a semi-automated method to classify and identify the waveforms, we performed PCA with k-means clustering to determine the most common baseline waveform templates for putative Type 2 and 3 events (Supplementary Fig. 8). These waveform templates became the basis of a template matching algorithm to detect and identify individual Type 2 and Type 3 events throughout the recordings. The criteria for identifying Type 2 and 3 events were: 1) absolute waveforms were greater than 25 μV; 2) detected waveforms correlated above 0.8 with the template event waveform; 3) the second derivative at the waveform onset was greater than 2; and 4) the absolute average voltage in the 100 ms preceding the event onset was less than 25 μV (to reduce the chances of capturing ongoing oscillations) (Fig. 3F,G; see Materials and Methods). The code for using these criteria to detect such events in other recordings is available for use by the community (https://github.com/Center-For-Neurotechnology/LFP-Type2-and-Type3-Detection).

Our results confirmed that our template matching approach could both detect and separate Type 2 and 3 events. More specifically, we found that the average time constant rise time ($\tau_{\text{rise time}}$) and time constant decay time ($\tau_{\text{fall time}}$) were significantly different between event types, after we averaged values per patient and then compared between types ($N = 36$; $P < 0.00001$; Wilcoxon rank-sum test; Supplementary Fig. 9). Type 2 events had an average time $\tau_{\text{rise time}}$ of 14.18 ± 8.42 ms and an average $\tau_{\text{fall time}}$ of 30.62 ± 6.33 ms as averaged across participants (after taking the absolute voltage values, see Materials and Methods). In contrast, Type 3 events had an average $\tau_{\text{rise time}}$ of 28.62 ± 8.80 ms and $\tau_{\text{fall time}}$ of 81.48 ± 11.91 ms. More importantly, Type 3 events were significantly more frequent than Type 2 events ($P < 0.0001$; Wilcoxon rank-sum test; Fig. 3H; Supplementary Fig. 9), with Type 3 events ($n = 55\,406$) occurring ~9 times more often than Type 2 events ($n = 6404$) across recordings and participants. To demonstrate that these events repeated in time and space, we calculated the detected Type 2 and 3 events' variance within and across channels to determine waveform consistency through time on the same channels. If there was less variance in the waveform within

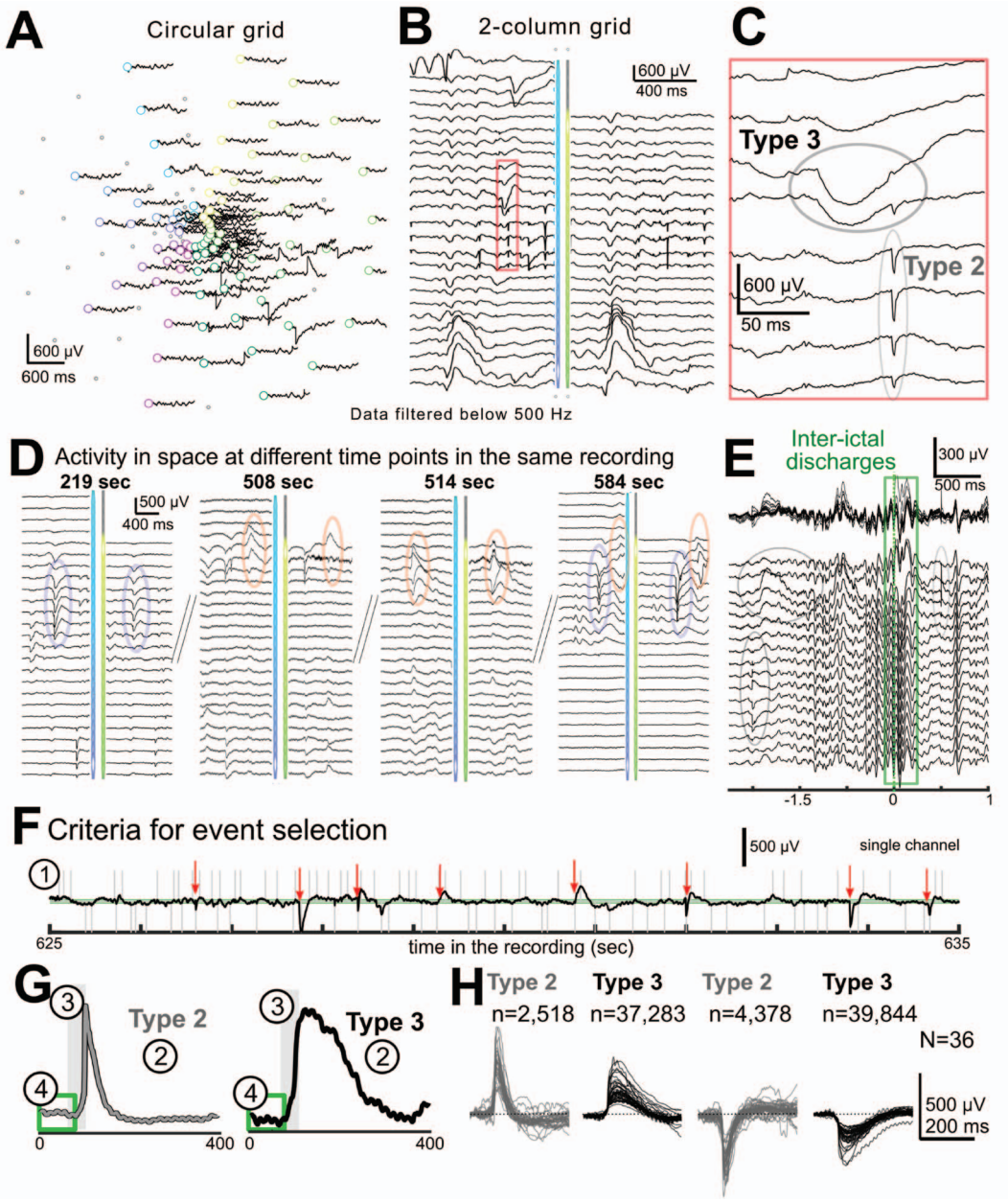

Figure 3. Classifiable events can be identified across recordings and participants. (*A*) Recording from participant IP25, mapped to the circular grid. Waveform color-coding matches channel color-coding with cyan to magenta (channels 1–64) and green to yellow (channels 65–128) indicating the four separate 32-channel amplifier banks used in the recording (Bank A: 1–32; Bank B: 33–64; Bank C: 65–96; Bank D: 97–128). Only the channels that fulfilled the criteria are shown as nongray dots. (*B*) Example recording (electrodes that fulfilled criteria represented as nongray dots) from participant IP15 showing activity changes in time, mapped to the 2-column electrode array. (*C*) Zoomed view of the red box in *B* showing Type 2 and 3 events. (*D*) Example recordings of events at different time points (for IP15) showing only a subset of electrode channels. Repeated events through time for two different event examples are shown (orange and blue ovals). (*E*) Example recordings (IP11) of a detected IID, indicated by a green rectangle, along with Type 2 and 3 events (circled in gray). (*F*, *G*). Stepwise criteria to detect Type 2 and 3 events, with template waveforms shown in *G*. (1) The first step detected absolute peaks that are greater than 25 µV, as shown in example traces from a single channel and case (IP15). Gray vertical lines denote detected cross-threshold peaks, green lines the thresholds. Red arrows show the events that fulfill all four selection criteria. (2) The next step detected peaks that correlate with the templates ≥0.80. (3) Selected events had a second derivative greater than 2 in the time period at onset, indicated by the shaded gray box. (4) Finally, waves were kept if they had no large deflections before event onset, that is, within 100 ms before crossing the 25-µV threshold, indicated by the green boxes. (*H*) Average waveforms per participant ($N = 36$) for the different event classes. The dotted lines indicate the zero-crossing value, in microvolts, to illustrate the number of positively (two left columns) and negatively (two right columns) deflecting detected waveforms. All voltage data shown were low-pass filtered using the high cut-off frequency of 500 Hz.

a channel versus between channels, then these events could be repeated through time on the same channel. The voltage variance across channels was larger than within channels (Supplementary Fig. 9). While this difference was not significant ($P > 0.05$, Wilcoxon rank-sum test, Supplementary Fig. 9), our combination of template matching and event detection criteria reduced detected waveforms' variance between and across channels.

In multiple participants, we confirmed the presence of Type 2 and Type 3 events in various brain regions by sampling across brain regions, between cases, and, in 12 instances, when moving the electrode to different brain areas during recording (Supplementary Figs 1–3 and 5). There were no significant differences among recordings in the temporal lobe, dlPFC, motor area (precentral gyrus), and parietal lobe ($P > 0.3320$; Kruskal–Wallis multiple comparison test). We did not observe significant differences in waveform shapes and overall frequency during baseline recordings between the epilepsy and tumor surgery contexts or between awake and anesthetized patients ($P > 0.05$; Wilcoxon rank-sum test; Supplementary Figs 1, 2 and 9). These results could mean that anesthesia does not change the elemental properties of neuronal communication but might have a dynamic impact on frequency and distribution of those events. These events were detectable using different recording systems with the same electrodes (see Materials and Methods). In addition, we found almost no Type 1, 2, or 3 events when recording over putative tumor tissue; when we flipped the array upside down so that the electrode pads were not facing the pial surface ($N = 1$ in each case, see Materials and Methods); or when placed in saline (Supplementary Figs 10–12).

Finally, we compared the Type 2 and 3 events to the IIDs detected in our recordings (Fig. 3E). Of the 37 PEDOT:PSS recordings, only 31 underwent processing, via automated systems combined with visual inspection, to identify IIDs (Janca et al. 2015). Interestingly, 15 of these 31 recordings had no detectable general IIDs but did include Type 2 and 3 events. Of the PEDOT:PSS recordings with detectable IIDs, the IIDs did not correlate with combined Type 2 and 3 events on the per-participant level (rho = 0.35, $P = 0.17$). Finally, we rarely found visible overlap between Type 2 and 3 events relative to the detected IIDs on a per-IID level (Fig. 3E).

Event Types 1, 2, and 3 have different spatial characteristics

Type 2 and 3 events spanned multiple channels (Figs 1–3). We examined the spatial spread of concurrent Type 2 and 3 events with onset times within the same10-ms time window (chosen based on IEI distributions; Fig. 4A,B). For windows in which multiple channels detect one event, we measured the average number of reporting channels, spatial distance from the first to the last reporting channel (in µm), area covered (in μm^2), speed of waveform travel (in m/s), and event time span (in seconds). None of these parameters significantly differed between Types 2 and 3, though multichannel Type 3 events tended to cover more area and longer spatial distances ($P > 0.07$; Wilcoxon rank-sum test; Fig. 4B). Using this approach, we found that Type 2 and 3 events were observed, on average, across 5–10 channels across the entire array. This was equivalent to or slightly more than a 100 µm × 100 µm area, suggesting that these events are relatively localized (Fig. 4B). However, the detected Type 3 events spread significantly faster (Type 2: 0.05 ± 0.038 m/s; Type 3: 0.08 ± 0.0511 m/s; $P = 0.005$; rank-sum = 405; Wilcoxon rank-sum test) Fig. 4B,iv). The spatial spread differences between the larger circular grid and the smaller 2-column grid (as indicated by the white vs. black scatter plots; Fig. 4B,ii,iii) likely produced the considerably varied event speeds per participant (Fig. 4B,iv).

Type 2 and 3 Events Are Detectable with Other Microelectrode Types and Near the Cortical Surface

To determine if these events are only present in PEDOT:PSS recordings from the cortical surface, we applied our template matching to concurrent clinical electrodes (3-mm diameter contacts on the brain surface; $N = 9$). We found almost no Type 2 ($n = 12$; 0.0027 ± 0.0061 events per second) or Type 3 ($n = 75$; 0.0167 ± 0.0287 events per second) events on the clinical electrodes, which was significantly fewer than in concurrent PEDOT:PSS recordings (Type 2: $n = 1383$; 0.31 ± 0.34 events per second; Type 3: $n = 12\,182$; 2.71 ± 3.28 events per second; $P < 0.002$ for both Type 2 and 3; Wilcoxon rank-sum test; Fig. 4C,i). The clinical leads could be summing activity from a much larger area effectively raising the overall background activity level such that these highly localized, and bidirectional, events disappear.

While the Type 2 and 3 events were not easily observed with clinical electrodes, we tested whether we could detect these events with other neurorecording systems. To this end, we performed the same template matching on neural recordings from patients with epilepsy semi-chronically implanted with Utah arrays, which were either 1 mm ($N = 4$) or 1.5 mm ($N = 4$) deep (Fig. 4C,ii; Supplementary Table 3). We found that the Utah array recordings were noisier than the PEDOT:PSS recordings, so we increased our correlation threshold for identifying Type 2 and 3 events from 0.8 to 0.9, to be stricter in our detections. Even with this more strict detection approach, we found more Type 2 and 3 events with the shorter Utah electrodes (Type 2: $n = 76$; Type 3: $n = 4369$) than the deeper ones (Type 2: $n = 14$; Type 3: $n = 111$) using the same template matching as in the PEDOT:PSS data analysis (Type 2: $P = 0.08$; Type 3: $P = 0.083$; Type 2: 1.0 mm- 0.0079 ± 0.0028 vs. 1.5 mm- 0.0015 ± 0.0008 per second; Type 3: 1.0 mm- 0.4551 ± 0.2818 vs. 1.5 mm- 0.0116 ± 0.0067 events per second; $N = 4$ each Utah array depth; Wilcoxon rank-sum test; Fig. 4C,ii). We also used the same template-matching approach on semi-chronic laminar microelectrode data that sample multiple cortical layers (Ulbert, Halgren, et al. 2001a; Ulbert, Karmos, et al. 2001b; $N = 9$; Fig. 4C,iii). We observed few Type 2 events in the laminar recordings ($n = 24$; 0.002 ± 0.002 events per second) but more Type 3 events ($n = 3084$, 0.26 ± 0.46 events per second). Interestingly, the laminar recordings yielded more Type 3 events in the superficial cortical layers, as evidenced by the average negative correlation between channel numbers and Type 3 counts across the array (rho = −0.48 ± 0.38; significantly different to zero; $P = 0.0313$; Wilcoxon signed rank test; $N = 9$; Fig. 4). To summarize, Type 2 and 3 events were detectable by methods other than PEDOT:PSS microelectrodes, including semi-chronic electrodes, and occurred more often in superficial cortical layers.

Finally, as a separate check to determine if these events can be found in yet another set of intracranial recordings in the human cortex, we applied our automatic Type 2 and 3 event detector to single electrode recordings lowered through the dlPFC as is done to locate subcortical deep nuclei for DBS electrode implants (Patel et al. 2013; Jamali et al. 2019). We additionally found both Type 2 and 3 events in these recordings ($N = 2$ patients, data not shown).

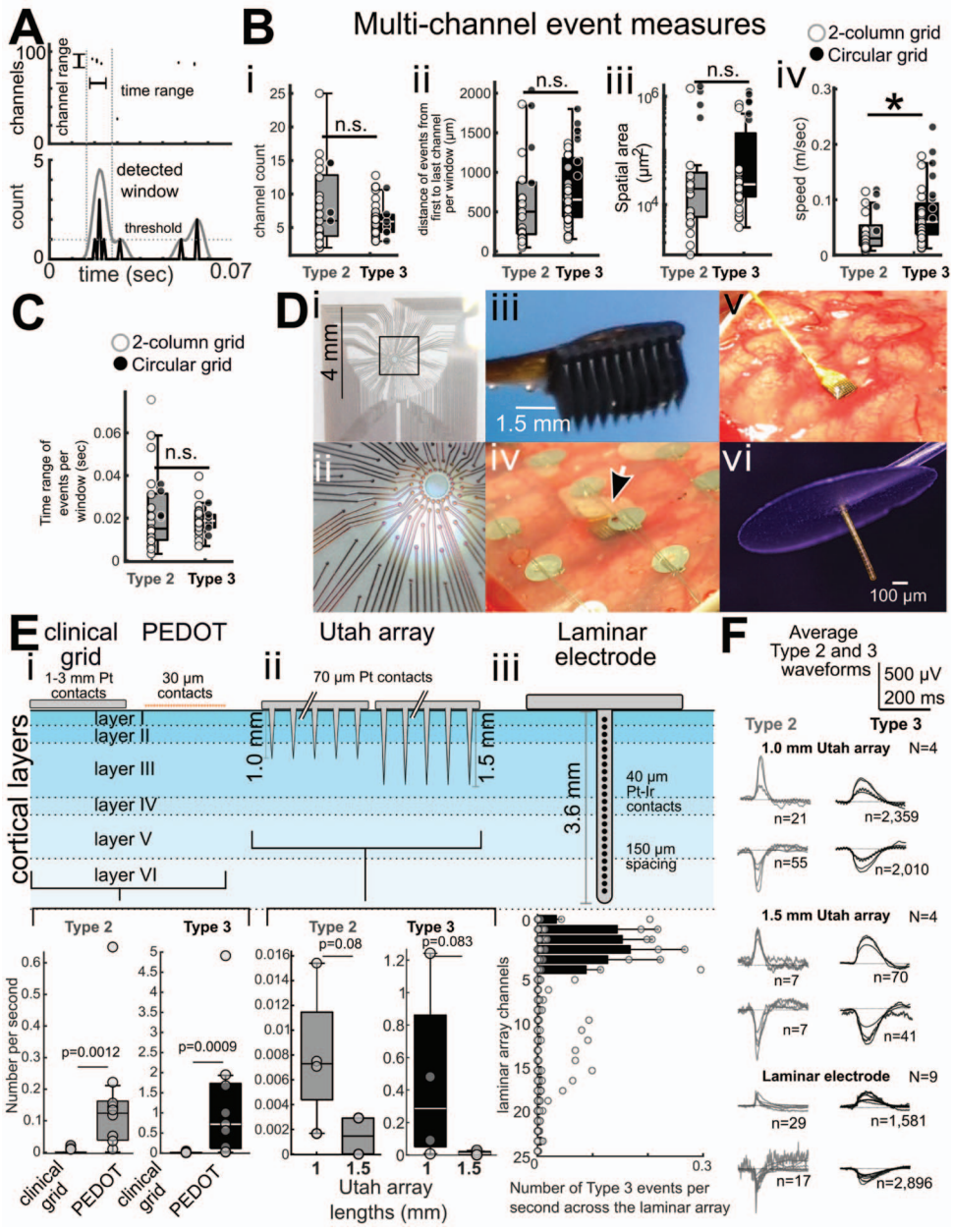

Figure 4. Temporal and spatial spread of Type 2 and 3 events. (*A*) Example recording from participant IP17 illustrating methods for determining event spatial spread (area). (*B*, i–iv) In cases where multiple channels detected one event, we compared the detected waveforms across channels, area covered (μm^2), speed of event propagation across channels (m/s), and distance traveled across the electrode array (μm). Box plots and confidence intervals around the mean values per measure per participant are indicated by whisker bars; center line indicates median, $N = 36$. (*C*) Event time span (s). White dots are the 2-column grids, while black dots are the circular grid recordings per participant. Asterisks indicate $P < 0.05$, Wilcoxon rank-sum test. (*D*) Images of the circular PEDOT:PSS grid electrode (*D*, i, ii), Utah array (*Diii–iv*), implanted electrode (arrowhead) overlaid by a clinical grid (*Div*), the implanted electrode (*Dv*), and a laminar array electrode (*Dvi*). (*E*, i–iii) Top: diagrams of the clinical surface electrodes, PEDOT:PSS array, Utah laminar arrays (1.0- and 1.5-mm depths), and laminar arrays showing relative sampling geometry of the different systems. Bottom: (*E*, i) Significantly more Type 2 and 3 events per second occur in the PEDOT:PSS array recordings than the clinical recordings ($P < 0.001$; $N = 9$; Wilcoxon rank-sum test). (*E*, ii) Significantly more Type 2 and 3 events are detected per second in the shallower Utah array recordings than the deeper recordings ($P < 0.001$; $N = 4$ each Utah array depth; Wilcoxon rank-sum test). (*E*, iii) More Type 3 events are detected per second in superficial laminar contacts as evidenced by the average negative correlation between the channel number and Type 3 counts across the array (rho = −0.48 ± 0.38; significantly different from zero; $P = 0.0313$; Wilcoxon signed rank test; $N = 9$). (*F*) Example average detected Type 2 and 3 events per participant with n = number of detected events. The dotted lines indicate the zero-crossing value in microvolts to illustrate the number of positively and negatively deflecting detected waveforms. In *B*, *C*, and *E*, the number of events were first averaged per contact and then averaged per patient. Each dot in *B*, *C*, and *E* represents this average for an individual participant.

Spectral Dynamics Surrounding Type 1, 2, and 3 Events

We performed four separate analyses to specifically determine if any of the detected events were part of an ongoing oscillation (Cole and Voytek 2017). We examined 1) event-locked spectral power increases surrounding the events (performed for Type 1, 2, and 3 events); 2) peaks in power for oscillations at specific frequency bands surrounding each event (after removing the events, performed for Type 2 and 3 events, including with shuffled trials); 3) phase-locking of Type 2 and 3 events with specific frequency bands (after removing the events, performed for Type 2 and 3 events); and 4) periodic regularity in the IEI and autocorrelation plots (performed for Type 1, 2, and 3 events). We focused on recordings of spontaneous activity without additional stimuli or manipulations and on five different frequency bands (2–4, 4–8, 8–15, 15–30, 30–55, and 65–200 Hz). Regarding power changes surrounding events, phase-locking measures, and periodic regularity in the IEI dynamics, see the Supplementary Material (Supplementary Figs 13–17). Throughout these analyses, we found no significant relationship in phase or power between ongoing oscillations and Type 2 and 3 events.

All three event types were associated with a broadband increase in power during the event or slightly beforehand (~0.25 s) in the event-triggered normalized power dynamics (Supplementary Fig. 13). Type 1 events coincided with an average broadband increase in power for the event duration on multiple frequency bands (4–30 Hz) (Supplementary Fig. 13). Type 2 events coincided with a significant broadband increase in power slightly before and during the event ($P < 0.001$; Wilcoxon rank-sum test; corrected for multiple comparisons with false discovery rate control; Supplementary Fig. 13). Type 3 event-triggered LFP power had low-frequency power peaks surrounding each event, but within 0.25 s, which were smaller than the change in power during the Type 2 events (Supplementary Fig. 13). Outside the 0.25-s window, no consistent power modulation in any frequency band preceding the events in the event-triggered power dynamics. We found no clear relationship between ongoing oscillations relative to Type 2 and 3 events. We did not test the spectral relationships between Type 2 and 3 events relative to external stimuli, as we sought to study Type 1, 2, and 3 events relative to ongoing oscillations that are not stimulus-linked. More importantly, Type 2–3 events' relationships to spectral dynamics are outside the scope of this study and will be part of future research, particularly in other species.

Confounding these results, however, is that these significant changes in power could be because the sharp deflection at the onset of the Type 1, 2, and 3 events generates a broadband increase in power in all frequencies. To test this, we performed the same event-triggered power calculation on the very few artificial "events," from saline recordings, which were detected using our template matching approach but did not have as sharp waveform onsets. These events had no such power increase at onset (Materials and Methods, Supplementary Fig. 14).

Type 1–3 Events Are Not a Purely Human Phenomenon and Are Present in Healthy Cortex

To determine if these events represent normal neural activity, as they could be small-field IIDs in epileptiform tissue (Curtis et al. 2012), and to prepare for future, more extensive mechanistic investigations (Barry 2015; Moore et al. 2017; Suzuki and Larkum 2017; Abdelfattah et al. 2019), we sought these events in animal recordings with PEDOT:PSS electrode arrays. These studies included recordings from the barrel cortex region of the primary somatosensory cortex (S1) in alpha-chloralose anesthetized mice ($N = 4$), the primary visual cortex (V1) in a ketamine-anesthetized mouse, the primary visual cortex (V1) in two isoflurane-anesthetized mice, and both primary and higher visual areas (VI and V4) in an anesthetized NHP in an acute setting ($N = 1$) using the circular, 2-column, and square grid PEDOT:PSS electrodes (Supplementary Figs 4, 5, 18; Supplementary Table 4). In both the NHP and mouse barrel cortex, where the array was placed directly on the cortical surface (with the dura removed), we found Type 1, 2, and 3 waveforms across recording sessions performed with different electrodes as well as repeatedly in the same recording sessions. In the V1 mouse epidural recording session, where the array was placed on top of the dura, we found only Type 2 and 3 waveforms, possibly due to the low-pass filtering property of the dura (Supplementary Fig. 18; Type 1 activity data not shown). The Type 2 and 3 events all had waveform characteristics ($\tau_{\text{rise time}}$ and $\tau_{\text{fall time}}$) and frequencies similar to those observed in the human recordings (Supplementary Figs 18–20). We also performed event-triggered spectral comparisons and found dynamics similar to those in humans (Supplementary Fig. 20). As a final test, we performed postmortem recordings in the V1 area of cortex in a mouse that had been anesthetized with ketamine. We found that the Type 1, 2, and 3 waveforms had completely disappeared after euthanasia, supporting their physiological origin (Supplementary Fig. 18).

Auditory Stimulation Type 3 Event Frequency

To test if these events were relevant to neural processing during behavior, we recorded neural activity over the human superior temporal gyrus (STG) and lateral prefrontal cortex while presenting regular auditory cues in a subset of participants undergoing awake resective surgeries (Ganji, Atsunori, et al. 2017a; Ganji, Kaestner, et al. 2017b; Hermiz et al. 2018) ($N = 11$; Fig. 5A). We detected both evoked potentials and Type 1–3 events related to the auditory task (Fig. 5B; see Materials and Methods). When we performed the PSTH calculations for Type 1–3 events, we found that Type 3 events were the most frequent following the auditory stimulus (Fig. 5B), with no significant difference in counts between Type 1 and Type 2 events (Fig. 5B, event rate (Hz) comparison: $P = 0.1078$; Wilcoxon rank-sum test). The evoked potentials tended to be time-locked across trials and were slower, while the Type 3 event onsets were more varied in the half second after sound began (note the varying peaks in the PSTH in Fig. 5B). Further behavioral and auditory stimuli may be needed to better delineate these dynamics, particularly since spectral analyses have shown notable changes in high gamma and other frequency bands in response to auditory stimulation over the STG intraoperatively using PEDOT:PSS (Hermiz et al. 2018). Additionally, waveform characteristics did not vary significantly during the auditory cue versus noncue epochs (Supplementary Fig. 21).

Pharmacological Manipulation Alters Event Rate

We hypothesized that if these events are physiological, then Type 1, 2, and 3 event rates should vary with cold saline application ($N = 8$) or intravenously administered proconvulsant agents (methohexital or alfentanil), which are used to map seizure foci in the brain (Curtis et al. 2012) ($N = 9$; Supplementary Table 1). Across participants, both cold

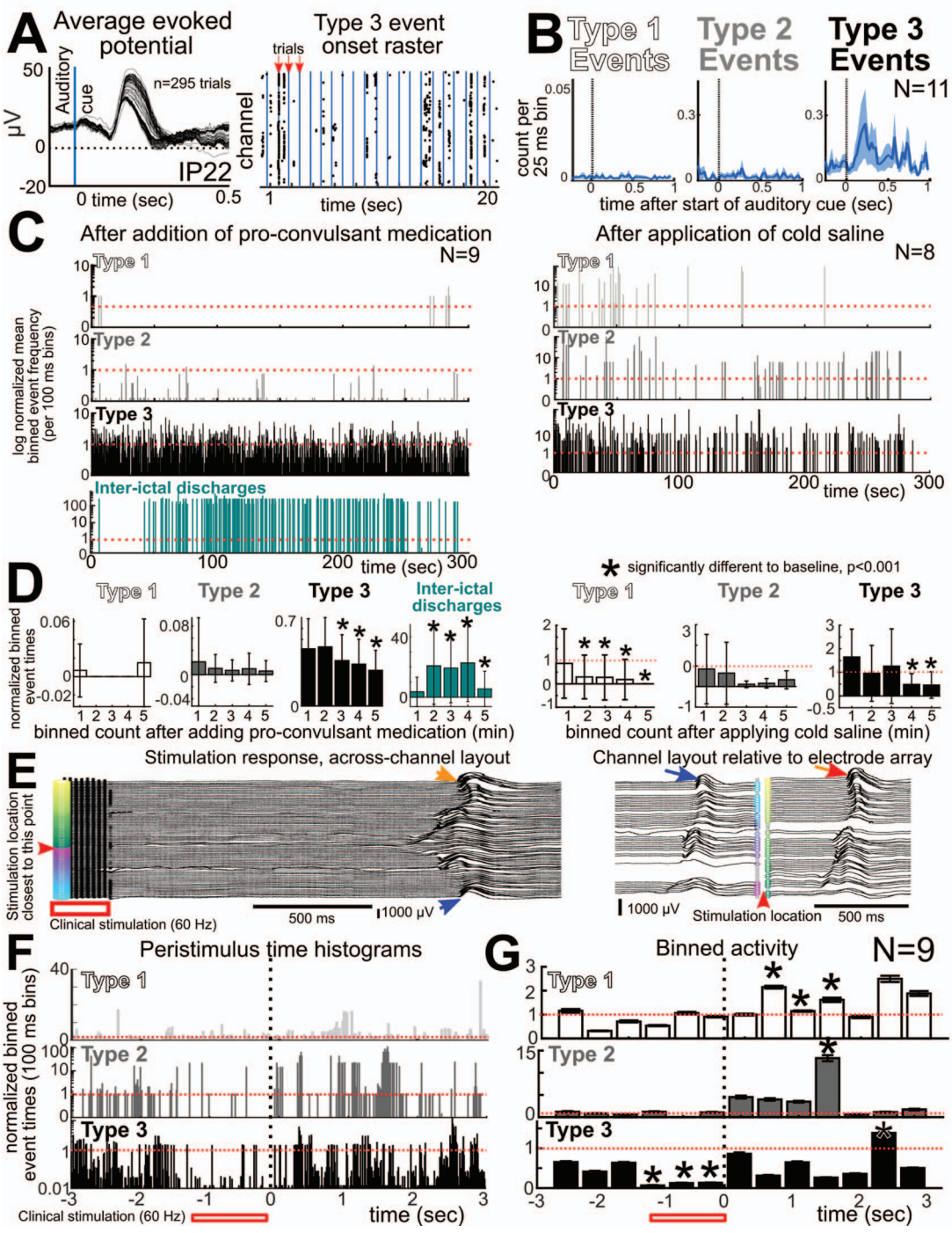

Figure 5. Manipulations alter rates of Type 1–3 events. (*A*) Effects of auditory stimuli on Type 2 and 3 events. Left: Recording from participant IP22 showing neural dynamics during repeated auditory stimuli in the averaged evoked potentials across trials. Right: Raster plots of Type 3 events occurring across all trials with auditory stimulus trial times indicated by blue vertical lines. (*B*) Left: PSTHs of each event type binned per 25 ms and then averaged across all patients ($N = 11$). For the line plots, shaded error regions are all SEM. (*C*) Effects of pro-convulsant medication and cold saline on Type 1–3 events and IIDs. PSTH of log binned activity following the administration of pro-convulsant medication (methohexital or alfentanil; left) or cold saline application (right) averaged across patients. Type 1 (top), Type 2 (middle), and Type 3 events (middle) as well as IIDs (bottom) were binned every 100 ms and normalized relative to baseline by dividing each bin by the average baseline activity. The dotted red line is the baseline normalization value. (*D*) Histogram of activity changes with 5-min bins. Error bars are SEM, $N = 9$ for pro-convulsant medication, $N = 8$ for cold saline application. Asterisks indicate significant difference from baseline with $P < 0.001$, Wilcoxon rank-sum test. (*E*) Electrical stimulation changes in the rate of Type 1–3 events. Recording from participant IP07 showing a wave of activity (Type 3 event) following a train of stimuli delivered at 60 Hz for 1–2 s during clinical mapping, with the channels laid out along a single line (left) and time-voltage curves mapped relative to the 2-column grid electrode layout (activity in space, right). Blue and orange arrowheads indicate the same pair of channels as in the left time-voltage plots versus the right time-voltage plots relative to the electrode layout. The red arrowhead indicates the direction of stimulation relative to the electrode layout, though the bipolar stimulation was 1–2 cm away. (*F*) PSTHs of binned activity

saline and pro-convulsant medication such as methohexital suppressed event frequency (Fig. 5C,D). Administering pro-convulsant medication notably lowered Type 2 and 3 event rates while still increasing epileptiform activity. More specifically, Type 2 events tended to decrease 4 min after the addition of pro-convulsant medication ($0.0.0096 \pm 0.0772$ Hz vs. 0.02 ± 0.219 Hz before) ($P = 0.033$; $N = 9$; Kruskal–Wallis multiple comparisons test). Type 3 events were significantly less frequent 3 min after pro-convulsant medication was intravenously injected (0.52 ± 0.813 Hz before injection vs. 0.38 ± 0.678 Hz 4 min after injection and continuing up to 5 min; $N = 9$; $P < 0.0001$; Kruskal–Wallis multiple comparisons test; Fig. 5C,D, left column). Type 1 events were only found in 1 of the 9 recordings with pro-convulsant medication, so we could not perform the same statistical comparisons.

We contrasted these results with changes in the rate of IIDs as identified by trained epileptologists. IIDs were significantly more frequent after intravenous injection of pro-convulsant medication (0.001 ± 0.001 Hz before injection vs. 0.0099 ± 0.0094 Hz 3 min after injection; $N = 9$; Fig. 5C,D, left column), adding further evidence that these events belong to a healthy electrophysiological repertoire of neural activity rather than miniature IIDs (Schevon et al. 2008, 2010).

Adding cold saline suppressed Type 1, 2, and 3 events across participants ($N = 8$; Fig. 5C,D). Type 1 event counts dropped significantly, from 0.0029 ± 0.0023 to 0.0001 ± 0.0002 Hz 2 min after cold saline application ($P < 0.0001$; Kruskal–Wallis multiple comparisons test). Type 2 event rate decreased from 0.01 ± 0.024 Hz during baseline to 0.002 ± 0.003 Hz 2 min after cold saline application across all channels and all participants, though the change was not significant ($P = 0.7282$; Kruskal–Wallis multiple comparisons test). Cold saline also rendered Type 3 events less frequent, with a significant decrease after 2 min (0.04 ± 0.046 Hz before addition of cold saline vs. 0.01 ± 0.019 Hz 2 min after saline addition; $P < 0.0001$; Kruskal–Wallis multiple comparisons test; Fig. 5C,D, right column).

It should be noted that neither intervention significantly altered waveform characteristics relative to baseline ($P > 0.12$; Wilcoxon rank sum test; Supplementary Fig. 21). Additionally, in all cases, room temperature saline was regularly used to irrigate the cortical surface during surgery, and event rates did not change during application of room temperature saline (data not shown).

Electrical Stimulation Changes Event Rates and Spread

To further test the hypothesis that Type 1–3 events have neural origins, we examined changes in activity during and after trains of electrical stimuli (as in motor or language mapping; Berger and Ojemann 1992; Mueller and Morris 1993; Kawaguchi et al. 1996; Viventi et al. 2011; Borchers et al. 2012; Fig. 5E). When stimuli trains were applied to the cortex surface, consequent traveling waves of Type 3 events progressed across all channels, sometimes starting soon after stimulation ended but often initiating 1–2 s after stimulation (Fig. 5E). These propagating waves of activity occurred all instances with clinically relevant trains of electrical stimulation. Similar activity waves were reported in other situations in other cortical recordings (Viventi et al. 2011), though not due to stimulation.

We examined the PSTH of Type 1–3 events around each stimulation train (normalized to 1 s before stimulation) and found that, during stimulation, Type 2 event rate decreased and Type 3 events were significantly inhibited ($P < 0.0001$; Wilcoxon rank-sum comparison between baseline and each binned time window; Fig. 5F,G). Immediately after stimulation, Type 1, 2, and 3 events were all more frequent ($P < 0.0001$; Wilcoxon rank-sum comparison between baseline and each binned time window; Fig. 5F,G), while waveform characteristics were unchanged (Supplementary Fig. 21).

Temporal Interactions between Different Event Types

While investigating we examined whether Type 1 events had a consistent relationship to the slower Type 2 and 3 events (Fig. 6), we found several examples across participants where either Type 1, 2, and 3 events overlapped in time or Type 1 events preceded Type 2 or 3 events (Fig. 6A,B). Furthermore, we found small, but prominent, peaks in event cross-covariances with Type 1 events preceding Type 2 and Type 3 events, often by ~10 ms (Fig. 6C,D; $P < 0.0015$; Wilcoxon rank-sum test; $N = 36$). This small cross-covariance peak occurred between Type 2 and Type 3 events, though there was no significant lag between them (Fig. 6C,D; $P = 0.25$). Another way to measure the temporal relationship between events was to identify the maximum time lag between Type 1 events and Type 2 and Type 3 events for each recording and determine the count and distribution of the maximum lag. Again, we found a delayed peak around 10 ms between Type 1 and both Type 2 and 3 events (Fig. 6E). Interestingly, however, there were also a number of Type 3 events preceding Type 1 events at longer time scales (closer to 50–100 ms; $P < 0.0001$; Wilcoxon signed rank test for significant different to zero; $N = 24$; Fig. 6F). We also found notable deflection in the LFP around Type 1 events (after normalizing relative to 0.5 s before the fast event) across participants ($P < 0.05$, false discovery rate controlled; $N = 24$; Supplementary Fig. 22). Together, these findings suggest that Type 1 events generally occur prior to Type 2 and 3 events, on the ~10-ms time scale.

Discussion

We observed repeated, localized microscale waveforms across both surface and penetrating microelectrode recordings in human and nonhuman cortex, and these waveforms could be divided into faster (~1 ms, Type 1) and slower (~10–100 ms, Type 2 and Type 3) events. To exclude possible artifacts of the recording system, electrodes, and other confounding factors, we examined recordings made in eight different centers; across 56 patients, four mice, and one NHP; and with four different recording systems. We found these events in all cases irrespective of the recording microelectrode type (PEDOT:PSS, Utah, laminar, and sharp electrodes) and under both acute and semi-chronic conditions. The different event types were selectively and separately inhibited by pro-convulsant medication and cold

around the time of stimulation (bar below figure) averaged across patients ($N = 9$, $n > 5$ trials per participant). Type 1 (top), Type 2 (middle), and Type 3 (bottom) events were binned every 100 ms and normalized relative to 1 s before stimulation. The dotted red line is the normalized baseline value. Note: the y-axis is in log-scaled increments. (G) Histograms of activity in 0.5-s bins before and after stimulation. P-values reflect differences between each 0.5-s bin per event type, $N = 9$; asterisks indicate significant difference from baseline with $P < 0.001$, Wilcoxon rank-sum test. Error bars are all SEM.

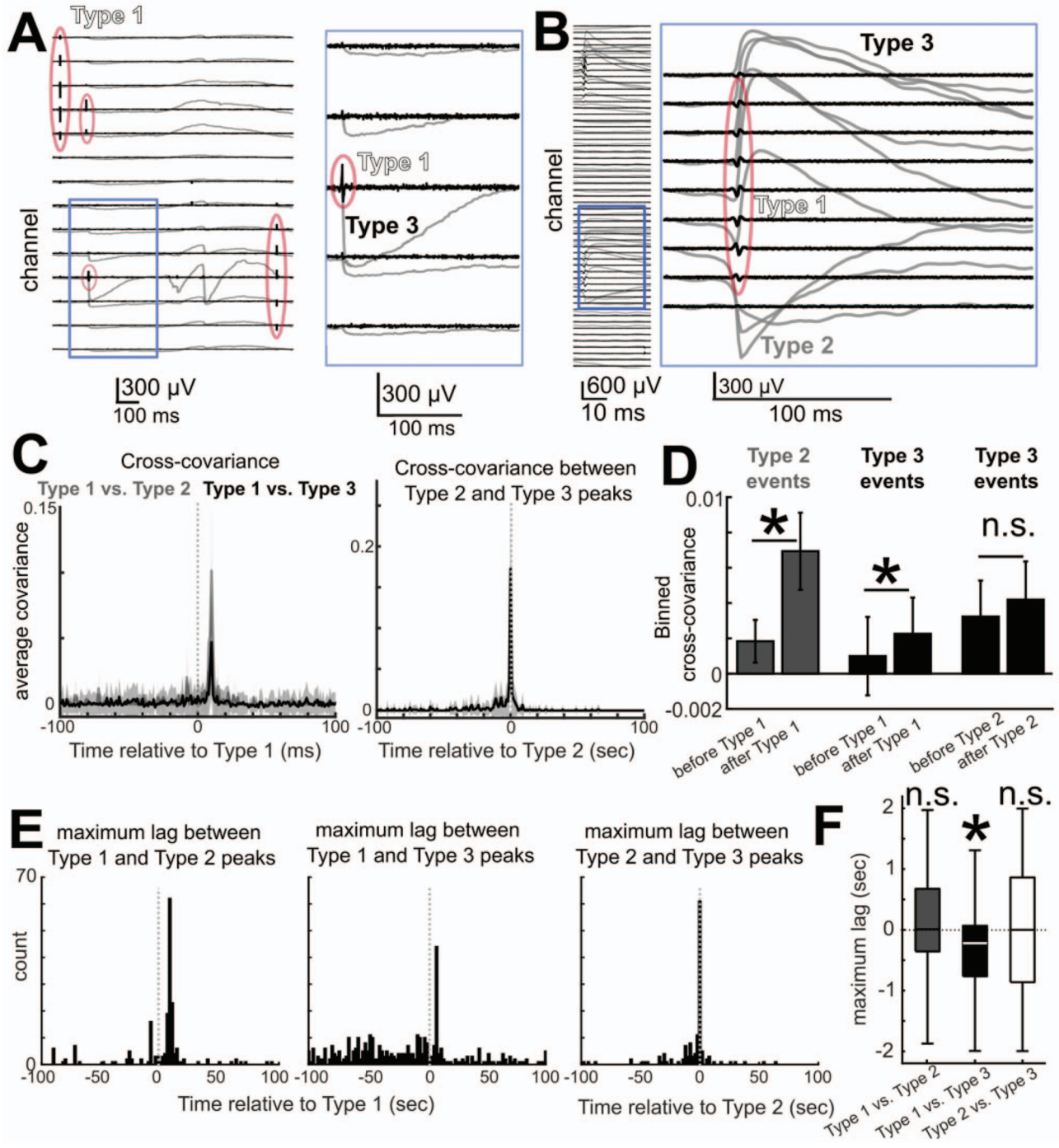

Figure 6. Temporal relationships between event Types. (*A*, *B*) Concurrent Type 1, 2, and 3 events across participants and channels in the simultaneous high-pass filtered data (between 250 and 6000 Hz, black lines) and the low-pass filtered data (at 500 Hz, gray lines). Type 1 events are circled in red. In A, Type 1 events are isolated from Type 2 and 3, and in B, a Type 1 event is on a different channel than the Type 2 event. (*C*) Left: Average cross-covariance plots between Type 1, 2 (gray line), and 3 (black line) events occurring simultaneously on different channels ($N = 24$). Right: Average cross-covariance plots between Type 2 and 3 event occurring simultaneously on different neighboring channels ($N = 36$). Shaded lines are standard error. (*D*) Average covariance from the 50 ms before each event to same interval after the event. Asterisks indicate $P < 0.001$; $N = 24$; Wilcoxon rank-sum test. Error bars are SEM. (*E*) Binned maximum time lag between the Type 1 event and the Type 2 and 3 events for all human recordings (two right plots) and the binned maximum time lag between the Type 2 and 3 events. (*F*) Median maximum lag in covariance between Types 1 and 2 (gray box plot), Types 1 and 3 (black box plot), and Types 2 and 3 with confidence bounds. Asterisk indicates that distribution differs significantly from zero, $P = 0.0004$. Wilcoxon signed rank test.

saline and were differentially impacted by electrical stimulation and sensory stimuli. In addition, we detected Type 2 and 3 events more often in the upper cortical layers, whether with shorter Utah arrays or the superficial contacts of laminar microelectrode arrays. Such events were essentially absent in both nonbiological recordings (e.g., recordings performed in saline, after euthanasia, or "upside down" meaning that the electrode was not facing the cortical surface) and concurrent neural recordings using 3-mm-diameter clinical macroelectrode contacts. Furthermore, these events had characteristic spatiotemporal patterns, were repeated and localized, and showed rare but statistically significant interactions, with Type 1 events more often preceding Type 2 and 3 events. Type 1, 2, and 3 events were suppressed with intravenous pro-convulsive medication.

Given that recordings in humans were performed during clinically necessary intracranial monitoring, a significant challenge for interpreting these results is the question of whether the Type 1, 2, and 3 events reflect normal brain activity or pathology. If these events were indeed related to abnormal brain activity, they would still be of interest as biomarkers of pathology; however, the present results provide substantial evidence that these are physiologically normal events. First, pathological events are unlikely to be induced by auditory stimuli and there was a clear separation between IIDs and these types of events. Second, we found these events in all examined patients regardless of their pathology or location and in semi-chronic recordings using Utah arrays and laminar recordings. Third, we observed similar events in both rodents and an NHP. Taken together, these findings strongly suggest that these events, recorded from the cortical surface, could be found in normal tissue and represent normal physiological activity.

Importantly, these surface events appeared as stand-alone occurrences with asymmetric waveforms and relatively fast kinetics but without rhythmicity, indicating that they were not part of typical ongoing oscillations. Were events part of an ongoing oscillation, we would expect a longer term increase in power before and after the event, either locked to the event onset or related to the phase of an ongoing oscillation. Yet, no significant power or phase relationships were observed between ongoing oscillations and these different events (background oscillations were observed separately from these discrete events). This indicates that these events occurred independently rather than as fragments of ongoing oscillations. While the events might have some relationship to oscillatory activity under certain circumstances, determining such a relationship would require specialized analysis focusing on a particular oscillation frequency band in a specific brain state or context, as in traditional analysis of single unit activity. Furthermore, we did observe more typical oscillations in these recordings, and, again, these were independent of the unitary events described here.

One caveat regarding the present work, however, is that our strict criteria and template matching likely under-sample Type 2 and 3 events. Thus, our interpretation of event rates and spatial characteristics might not be fully accurate. As has occurred with spike sorting, future work will need to evolve toward more sophisticated tools to detect these events in the course of spontaneous neural activity. An additional related potential confound is that most of the data are from acute recordings in the OR, an experimental arena prone to considerable noise and instability for electrophysiological recording. To mitigate these issues, we repeated the tests across hospitals, participants, species, electrodes, and recording systems. Concerned that the environment could be introducing noise, we also examined semi-chronic data to demonstrate the presence of these events. However, even with all these tests, we concede that some noise could be detected as events. Again, more sophisticated detection approaches could clear up these issues especially as we obtain a greater understanding of the cellular mechanisms underlying this activity. We hypothesize that the low impedance, conformable, spatially high-resolution PEDOT:PSS electrodes are better able to spatially map these events than rigid devices on the cortical surface, but this will require further testing.

While the cellular processes underlying these events are unknown and warrant further investigation, it is worth speculating on several possibilities. One is that the events reflect activity in specific, specialized, neural cell types present in supragranular layers of the cortex (Rakic and Zecevic 2003; Zaitsev et al. 2009; Mohan et al. 2015; Gabbott 2016; Boldog et al. 2018). These could include Cajal–Retzius cells or other relatively rare cell types found in upper cortical layers (Rakic and Zecevic 2003; Mohan et al. 2015; Gabbott 2016). Alternatively, these events could reflect ionic flux in glial cells in upper cortical layers, although the fast kinetics make this somewhat less likely as astrocytic waves normally occur on the time scale of seconds (Hassinger et al. 1996; Scemes and Giaume 2006; Takata and Hirase 2008; Kuga et al. 2011; Khakh and McCarthy 2015; Rouach et al. 2018). More intriguing is the possibility that some of the Type 1 and faster Type 2 events reflect back-propagating dendritic action potentials (Robbins et al. 2013; Stuart and Spruston 2015; Moore et al. 2017; Jia et al. 2019), while the slower Type 2 and Type 3 events could be the result of dendritic calcium spikes (Bakkum et al. 2013; Barry 2015; Suzuki and Larkum 2017). Similar activity has been reported using fine electrodes in freely behaving rats. In that instance, putative dendritic action potentials were recorded using tetrodes following the formation of a glial sheath, which increases contact between the neural dendrites and fine wires (Moore et al. 2017). The waveform shapes of extracellular dendritic action potentials reported in that study had similar voltage range (~0.5–1 mV) to the Type 2 events described here, although shorter duration (~5–10 ms). Type 2 and/or Type 3 events could also indicate localized calcium spikes in the apical tufts of pyramidal neurons from deeper layers (Ross 2015; Suzuki and Larkum 2017; Golding et al. 2018). Similar time courses and waveforms have also been recorded from the cortex surface in anesthetized rats, phenomena that were then verified, through optogenetics, laminar probes, pharmacological manipulation, and calcium imaging, as dendritic calcium spikes from layer 2/3 or layer 5 pyramidal neurons (Suzuki and Larkum 2017). Extrapolating from those findings and the data presented here, it is possible that high-density microelectrodes could be recording dendritic activity at the pial surface.

In addition, some of the Type 1 waveforms were well within the range of extracellular action potential dynamics as routinely recorded with other types of probes. Yet, the family of Type 1 events described here also included very narrow waveforms, some triphasic in appearance and some with relatively large amplitudes compared with previously recorded somatic action potentials. It should be noted that primate pyramidal neurons have been shown to produce fast (or "thin") spikes not often observed in nonprimate species (Vigneswaran et al. 2011). The different waveform shapes for the fast events we identified may also represent different neural subclasses (Bartho et al. 2004; Vigneswaran et al. 2011; Chan et al. 2014; Trainito et al. 2019). In addition, with their short duration and triphasic morphology, some Type 1 events resemble axonal action potential recordings

(Robbins et al. 2013; Stuart and Spruston 2015; Jun et al. 2017). In this scenario, some of the Type 1 events would reflect activity in unmyelinated axons in the uppermost cortical layers (Mohan et al. 2015). This notion is supported in part by the observed relationship whereby Type 1 events preceded some of the Type 2 and 3 events, thereby implying that the fast Type 1 events could be axon inputs while the slower events could be a post-synaptic consequence. These possibilities may also account for the fact that some Type 1 events were spatially colocalized with Type 2 and 3 events. While this colocalization was rare across recordings, the timing relationships were significant.

In summary, we speculate that these different classes of relatively fast activity could reflect a range of neuronal events including axonal action potentials, fast and slow events in the dendrite, and somatic action potentials. In the future, optical calcium and voltage imaging combined with electrophysiological recording approaches in animal models will be essential to further resolve the mechanisms of these events' generation (Harvey et al. 2009; Roome and Kuhn 2018; Abdelfattah et al. 2019; Adam et al. 2019; Chiang et al. 2020; Hossain et al. 2020). Electrophysiological events will need to be examined in awake animals using calcium imaging (Suzuki and Larkum 2017), intracellular recordings (Harvey et al. 2009; Abdelfattah et al. 2019), pharmacological interventions (Suzuki and Larkum 2017), and genetic cell-type-specific manipulation (Abdelfattah et al. 2019).

Exploring the entire neurophysiological signal from microelectrode technologies can uncover, or at least highlight, signals otherwise understudied in the neuroscience field. These results open the possibility that we can access circuit-level dynamics in the cortex using high-resolution sampling. More specifically, these Type 1–3 events could represent the entire input–output sequence of neuronal activity where, in a given brain region, there may be an incoming axonal volley (Type 1 events with very fast, trimodal waveforms), postsynaptic events (e.g., dendritic calcium spikes reflected as Type 2 and 3 events), followed by somatic action potentials (Type 1 events), and dendritic back-propagating spikes (Type 2), all in the setting of widespread activity measured by microelectrodes even on the surface of the cortex. If so, we could more thoroughly study the detailed neural circuit activity underlying physiological events and build more complete bridges from the single-cell level to large-scale population behavior in the context of both healthy and pathological human brain dynamics.

Supplementary Material

Supplementary material can be found at *Cerebral Cortex* online.

Author Contributions

Conceptualization: A.C.P., J.C.Y., S.S.C., S.A.D. Methodology: J.H., M.G., A.C.P., J.C.Y., S.S.C., S.A.D. Formal analysis: A.C.P., J.C.Y., D.J.S., M.H. Investigation: A.C.P., J.C.Y., D.R.C., N.R., K.K., S.B.R., S.W.L., D.M., S.I.F., P.S.J., B.V.N., S.B-H., A.M.T.R., D.S., D.P.C., I.U., D.F., O.D., J.R.M., D.L.S., E.N.E., J.L., S.K.B., Z.M.W., G.R.C., S.A.D., S.S.C. Resources: S.A.D., S.S.C., S.I.F., S.W.L., S.H.L., M.G., Y.G.R., H.O., L.H., J.L., Y.T. Data curation: A.C.P., D.J.S., J.C.Y., A.R.O. Writing: A.C.P., J.C.Y., S.S.C., S.A.D., D.P.C., Z.M.W., S.B.R., N.R., A.D., D.J.S., D.R.C., J.L., G.R.C., S.I.F., S.K.B., A.R.O. Visualization: A.C.P., D.J.S., M.H. Supervision: S.A.D., S.S.C. Project administration: A.C.P., J.C.Y., D.R.C., S.A.D., S.S.C. Funding acquisition: S.A.D., S.S.C., S.I.F., S.W.L., I.U.

Notes

We first would like to thank all the patients for their willingness to participate in this research. We thank Yangling Chou, Erica Johnson, Melissa Murphy, Aaron Tripp, Fausto Minidio, Alex Zhang, and Gavin Belok for help with data collection. We thank Laszlo Papp of Neuronelektrod Ltd, Budapest, Hungary, for the laminar array image. The views and conclusions contained in this document are those of the authors and do not represent the official policies, either expressed or implied, of the funding sources. *Conflict of Interest:* None declared.

Funding

The U.S. Army Research Office and Defense Advanced Research Projects Agency (Cooperative Agreement Number W911NF-14-2-0045); National Institutes of Health (Award Number 1F32MH120886) to D.R.C.; ECOR and K24-NS088568 to S.S.C.; Tiny Blue Dot Foundation (to S.S.C. and A.C.P.); and by an NSF-CAREER (award #1351980), NSF CMMI (award #1728497), an NSF-ECCS EAGER (award #1743694), and an NIH (award #DP2-EB029757) to S.A.D.; BRAIN Initiative (R01MH111359 to A.D.); and NIH (NEI R01-EY029022/EY023651 and NINDS U01-NS099700); the Dept. of Defense/CDMRP (VR170089) to S.B.R., S.W.L., and S.I.F.; the Hungarian Brain Research Program (2017-1.2.1-NKP-2017-00002) to I.U.

References

Abdelfattah AS, Kawashima T, Singh A, Novak O, Liu H, Shuai Y, Huang Y-C, Campagnola L, Seeman SC, Yu J, et al. 2019. Bright and photostable chemigenetic indicators for extended in vivo voltage imaging. *Science*. 365:699–704.

Amirnovin R, Williams ZM, Cosgrove GR, Eskandar EN. 2006. Experience with microelectrode guided subthalamic nucleus deep brain stimulation. *Neurosurgery*. 58:ONS96–102.

Adam Y, Kim JJ, Lou S, Zhao Y, Xie ME, Brinks D, Wu H, Mostajo-radji MA, Kheifets S, Parot V, et al. 2019. Voltage imaging and optogenetics reveal behaviour-dependent changes in hippocampal dynamics. *Nature*. 569:413–417.

Anastassiou CA, Perin R, Buzsáki G, Markram H, Koch C. 2015. Cell type- and activity-dependent extracellular correlates of intracellular spiking. *J Neurophysiol*. 114:608–623.

Bakkum DJ, Frey U, Radivojevic M, Russell TL, Müller J, Fiscella M, Takahashi H, Hierlemann A. 2013. Tracking axonal action potential propagation on a high-density microelectrode array across hundreds of sites. *Nat Commun*. 4:2181.

Barry JM. 2015. Axonal activity in vivo: technical considerations and implications for the exploration of neural circuits in freely moving animals. *Front Neurosci*. 9:1–12.

Bartho P, Hirase H, Monconduit L, Zugaro M, Harris KD, Buzsáki G. 2004. Characterization of neocortical principal cells and interneurons by network interactions and extracellular features. *J Neurophysiol*. 92:600–608.

Berens P. 2009. CircStat: a MATLAB toolbox for circular statistics. *J Stat Softw*. 31:1–21.

Berger MS, Ojemann GA. 1992. Intraoperative brain mapping techniques in neuro-oncology. *Stereotact Funct Neurosurg*. 58:153–161.

Boldog E, Bakken TE, Hodge RD, Novotny M, Aevermann BD, Baka J, Bordé S, Close JL, Diez-Fuertes F, Ding SL, et al. 2018.

Transcriptomic and morphophysiological evidence for a specialized human cortical GABAergic cell type. *Nat Neurosci*. 21:1185–1195.

Borchers S, Himmelbach M, Logothetis N, Karnath H. 2012. Direct electrical stimulation of human cortex—the gold standard for mapping brain functions? *Nat Rev Neurosci*. 13:63–70.

Cash SS, Halgren E, Dehghani N, Rossetti AO, Thesen T, Wang C, Devinsky O, Kuzniecky R, Doyle W, Madsen JR, et al. 2009. The human K-complex represents an isolated cortical downstate. *Science*. 324:1084–1087.

Cellot G, Lagonegro P, Tarabella G, Scaini D, Fabbri F, Iannotta S, Prato M, Salviati G, Ballerini L. 2016. PEDOT:PSS interfaces support the development of neuronal synaptic networks with reduced neuroglia response in vitro. *Front Neurosci*. 9:1–11.

Chan AM, Dykstra AR, Jayaram V, Leonard MK, Travis KE, Gygi B, Baker JM, Eskandar E, Hochberg LR, Halgren E, et al. 2014. Speech-specific tuning of neurons in human superior temporal gyrus. *Cereb Cortex*. 24:2679–2693.

Chiang CH, Won SM, Orsborn AL, Yu KJ, Trumpis M, Bent B, Wang C, Xue Y, Min S, Woods V, et al. 2020. Development of a neural interface for high-definition, long-term recording in rodents and nonhuman primates. *Sci Transl Med*. 12:1–13.

Cole SR, Voytek B. 2017. Brain oscillations and the importance of waveform shape. *Trends Cogn Sci*. 21:137–149.

Curtis MD, Jefferys JGR, Avoli M. 2012. Interictal epileptiform discharges in partial epilepsy: complex neurobiological mechanisms based on experimental and clinical evidence. In: *Jasper's basic mechanisms of the epilepsies*. 4th ed. Bethesda (MD): National Center for Biotechnology Information (US), pp. 1–24.

Delorme A, Makeig S. 2004. EEGLAB: an open source toolbox for analysis of single-trial EEG dynamics including independent component analysis. *J Neurosci Methods*. 134:9–21.

Dykstra AR, Chan AM, Quinn BT, Zepeda R, Keller CJ, Cormier J, Madsen JR, Eskandar EN, Cash SS. 2012. Individualized localization and cortical surface-based registration of intracranial electrodes. *Neuroimage*. 59:3563–3570.

Fabó D, Maglóczky Z, Wittner L, Pék Á, Eróss L, Czirják S, Vajda J, Sólyom A, Rásonyi G, Szucs A, et al. 2008. Properties of in vivo interictal spike generation in the human subiculum. *Brain*. 131:485–499.

Felsenstein O, Peled N. 2017. *MMVT–multi-modality visualization tool*. GitHub Repository.

Gabbott PLA. 2016. "Subpial fan cell"—a class of calretinin neuron in layer 1 of adult monkey prefrontal cortex. *Front Neuroanat*. 10:1–29.

Ganji M, Atsunori T, Gilja V, Halgren E, Dayeh SA. 2017a. Scaling effects on the electrochemical stimulation performance of Au, Pt, and PEDOT:PSS electrocorticography arrays. *Adv Funct Mater*. 27:1703019.

Ganji M, Kaestner E, John H, Nick R, Atsunori T, Daniel C, Heon LS, Snider J, Halgren M, Rees CG, et al. 2017b. Development and translation of PEDOT:PSS microelectrodes for intraoperative monitoring. *Adv Funct Mater*. 28:1700232.

Golding NL, Jung H, Mickus T, Spruston N. 2018. Dendritic calcium spike initiation and repolarization are controlled by distinct potassium channel subtypes in CA1 pyramidal neurons. *J Neurosci*. 19:8789–8798.

Halgren M, Fabó D, Ulbert I, Madsen JR, Eross L, Doyle WK, Devinsky O, Schomer D, Cash SS, Halgren E. 2018. Superficial slow rhythms integrate cortical processing in humans. *Sci Rep*. 8:1–12.

Halgren M, Ulbert I, Bastuji H, Fabó D, Eross L, Rey M, Devinsky O, Doyle WK, Mak-McCully R, Halgren E, et al. 2019. The generation and propagation of the human alpha rhythm. *Proc Natl Acad Sci USA*. 116:23772–23782.

Hamilton F, Berry T, Sauer T. 2018. Tracking intracellular dynamics through extracellular measurements. *PLoS One*. 13: 1–13.

Harvey CD, Collman F, Dombeck DA, Tank DW. 2009. Intracellular dynamics of hippocampal place cells during virtual navigation. *Nature*. 461:941–946.

Hassinger TD, Guthrie PB, Atkinson PB, Bennett MVL, Kater SB. 1996. An extracellular signaling component in propagation of astrocytic. *Proc Natl Acad Sci USA*. 93:13268–13273.

Hermiz J, Hossain L, Arneodo EM, Ganji M, Rogers N, Vahidi N, Halgren E, Gentner TQ, Dayeh SA, Gilja V. 2020. Stimulus driven single unit activity from micro-electrocorticography. *Front Neurosci*. 14:1–10.

Hermiz J, Rogers N, Kaestner E, Ganji M, Cleary D, Snider J, Barba D, Dayeh S, Halgren E, Gilja V. 2016. A clinic compatible, open source electrophysiology system. *Annu Int Conf IEEE Eng Med Biol Soc*. 2016:4511–4514.

Hermiz J, Rogers N, Kaestner E, Ganji M, Cleary DR, Carter BS, Barba D, Dayeh SA, Halgren E, Gilja V. 2018. Sub-millimeter ECoG pitch in human enables higher fidelity cognitive neural state estimation. *Neuroimage*. 176:454–464.

Hochberg LR, Serruya MD, Friehs GM, Mukand JA, Saleh M, Caplan AH, Branner A, Chen D, Penn RD, Donoghue JP. 2006. Neuronal ensemble control of prosthetic devices by a human with tetraplegia. *Nature*. 442:164–171.

Holmes CJ, Hoge R, Collins L, Woods R, Toga AW, Evans AC. 1998. Enhancement of MR images using registration for signal averaging. *J Comput Assist Tomogr*. 22:324–333.

Hossain L, Thunemann M, Devor A, Dayeh SA. 2020. Chronic 2-photon calcium imaging through transparent PEDOT:PSS microelectrode arrays in awake mice. In: *Biophotonics Congress: Biomedical Optics 2020 (Translational, Microscopy, OCT, OTS, BRAIN)*. *OSA Technical Digest*. Washington (DC): Optical Society of America. p. BW2C.2.

Jamali M, Grannan B, Haroush K, Moses ZB, Eskandar EN, Herrington T, Patel S, Williams ZM. 2019. Dorsolateral prefrontal neurons mediate subjective decisions and their variation in humans. *Nat Neurosci*. 22:1010–1020.

Janca R, Jezdik P, Cmejla R, Tomasek M, Worrell GA, Stead M, Wagenaar J, Jefferys JGR, Krsek P, Komarek V, et al. 2015. Detection of interictal epileptiform discharges using signal envelope distribution modelling: application to epileptic and non-epileptic intracranial recordings. *Brain Topogr*. 28:172–183.

Jia X, Siegle JH, Bennett C, Gale SD, Denman DJ, Koch C, Olsen SR. 2019. High-density extracellular probes reveal dendritic backpropagation and facilitate neuron classification. *J Neurophysiol*. 121:1831–1847.

Jun JJ, Steinmetz NA, Siegle JH, Denman DJ, Bauza M, Barbarits B, Lee AK, Anastassiou CA, Andrei A, Aydin Ç, et al. 2017. Fully integrated silicon probes for high-density recording of neural activity. *Nature*. 551:232–236.

Kaestner E. 2018. *A motor theory of reading: the interaction of visual and auditory language* [PhD thesis].

Kaiju T, Doi K, Yokota M, Watanabe K, Inoue M, Ando H, Takahashi K, Yoshida F, Hirata M, Suzuki T. 2017. High spatiotemporal resolution ECoG recording of somatosensory evoked potentials with flexible micro-electrode arrays. *Front Neural Circuits*. 11:1–13.

Kawaguchi M, Shimizu K, Karasawa J, Furuya H. 1996. Intraoperative myogenic motor evoked potentials induced by direct electrical stimulation of the exposed motor cortex under isoflurane and sevoflurane. *Anesth Analg*. 82:593–599.

Keller CJ, Truccolo W, Gale JT, Eskandar E, Thesen T, Carlson C, Devinsky O, Kuzniecky R, Doyle WK, Madsen JR, et al. 2010. Heterogeneous neuronal firing patterns during interictal epileptiform discharges in the human cortex. *Brain*. 133:1668–1681.

Khakh BS, McCarthy KD. 2015. Astrocyte calcium signaling: from observations to functions and the challenges therein. *Cold Spring Harb Perspect Biol*. 7:1–18.

Khodagholy D, Gelinas JN, Buzsáki G. 2017. Learning-enhanced coupling between ripple oscillations in association cortices and hippocampus. *Science*. 372:369–372.

Khodagholy D, Gelinas JN, Thesen T, Doyle W, Malliaras GG, Buzsáki G. 2015. NeuroGrid: recording action potentials from the surface of the brain. *Nat Neurosci*. 18:310–315.

Khodagholy D, Gelinas JN, Zhao Z, Yeh M, Long M, Greenlee JD, Doyle W, Devinsky O, Buzsáki G. 2016. Organic electronics for high-resolution electrocorticography of the human brain. *Sci Adv*. 2:e1601027.

Kuga N, Sasaki T, Takahara Y, Matsuki N, Ikegaya Y. 2011. Large-scale calcium waves traveling through astrocytic networks in vivo. *J Neurosci*. 31:2607–2614.

Mian MK, Sheth SA, Patel SR, Spiliopoulos K, Eskandar EN, Williams ZM. 2014. Encoding of rules by neurons in the human dorsolateral prefrontal cortex. *Cereb Cortex*. 24:807–816.

Mohan H, Verhoog MB, Doreswamy KK, Eyal G, Aardse R, Lodder BN, Goriounova NA, Asamoah B, Brakspear ABC, Groot C, et al. 2015. Dendritic and axonal architecture of individual pyramidal neurons across layers of adult human neocortex. *Cereb Cortex*. 25:4839–4853.

Moore JJ, Ravassard PM, Ho D, Acharya L, Kees AL, Vuong C, Mehta MR. 2017. Dynamics of cortical dendritic membrane potential and spikes in freely behaving rats. *Science*. 355:eaaj1497.

Mueller WM, Morris GL. 1993. Intraoperative and Extraoperative identification of eloquent brain using stimulation mapping. *Neurosurg Clin N Am*. 4:217–222.

Nordhausen CT, Rousche PJ, Normann RA. 1994. Optimizing recording capabilities of the Utah Intracortical Electrode Array. *Brain Res*. 637:27–36.

Oostenveld R, Fries P, Maris E, Schoffelen J-M. 2011. FieldTrip: open source software for advanced analysis of MEG, EEG, and invasive electrophysiological data. *Comput Intell Neurosci*. 2011:156869.

Pachitariu M, Steinmetz N, Kadir S, Carandini M, Harris K. 2016. Fast and accurate spike sorting of high-channel count probes with KiloSort. *Adv Neural Inf Process Syst*. 2016:1–9.

Patel SR, Sheth SA, Martinez-Rubio C, Mian MK, Asaad WF, Gerrard JL, Kwon C-S, Dougherty DD, Flaherty AW, Greenberg BD, et al. 2013. Studying task-related activity of individual neurons in the human brain. *Nat Protoc*. 8: 949–957.

Paxinos G, Franklin KBJ. 2001. *The mouse brain in stereotaxic coordinates*. San Diego: Academic Press.

Peled N, Gholipour T, Paulk AC, Felsenstein O, Dougherty DD, Widge AS, Eskandar EN, Cash SS, Hamalainen MS, Stufflebeam SM. 2017. *Invasive electrodes identification and labeling*. GitHub Repos. https://github.com/pelednoam/ieil.

Postelnicu G, Zöllei L, Fischl B. 2009. Combined volumetric and surface registration. *IEEE Trans Med Imaging*. 28:508–522.

Rakic S, Zecevic N. 2003. Emerging complexity of layer I in human cerebral cortex. *Cereb Cortex*. 13:1072–1083.

Reuter M, Rosas HD, Fischl B. 2010. Highly accurate inverse consistent registration: a robust approach. *Neuroimage*. 53:1181–1196.

Reuter M, Schmansky NJ, Rosas HD, Fischl B. 2012. Within-subject template estimation for unbiased longitudinal image analysis. *Neuroimage*. 61:1402–1418.

Rivnay J, Inal S, Collins BA, Sessolo M, Stavrinidou E, Strakosas X, Tassone C, Delongchamp DM, Malliaras GG. 2016. Structural control of mixed ionic and electronic transport in conducting polymers. *Nat Commun*. 7:1–9.

Robbins AA, Fox SE, Holmes GL, Scott RC, Barry JM. 2013. Short duration waveforms recorded extracellularly from freely moving rats are representative of axonal activity. *Front Neural Circuits*. 7:181.

Roome CJ, Kuhn B. 2018. Simultaneous dendritic voltage and calcium imaging and somatic recording from Purkinje neurons in awake mice. *Nat Commun*. 9:1–14.

Ross WN. 2015. Understanding calcium waves and sparks in central neurons. *Nat Rev Neurosci*. 13:157–168.

Rouach N, Dao Duc K, Sibille J, Holcman D, Holcman D, Rouach N. 2018. Dynamics of ion fluxes between neurons, astrocytes and the extracellular space during neurotransmission. *bioRxiv*. 4:1–18.

Scemes E, Giaume C. 2006. Astrocyte calcium waves: what they are and what they do. *Glia*. 54:716–725.

Schevon CA, Goodman RR, McKhann G, Emerson RG. 2010. Propagation of epileptiform activity on a submillimeter scale. *J Clin Neurophysiol*. 27:406–411.

Schevon CA, Ng SK, Cappell J, Goodman RR, McKhann G, Waziri A, Branner A, Sosunov A, Schroeder CE, Emerson RG. 2008. Microphysiology of epileptiform activity in human neocortex. *J Clin Neurophysiol*. 25:321–330.

Sessolo M, Khodagholy D, Rivnay J, Maddalena F, Gleyzes M, Steidl E, Buisson B, Malliaras GG. 2013. Easy-to-fabricate conducting polymer microelectrode arrays. *Adv Mater*. 25:2135–2139.

Sheth SA, Mian MK, Patel SR, Asaad WF, Williams ZM, Dougherty DD, Bush G, Eskandar EN. 2012. Human dorsal anterior cingulate cortex neurons mediate ongoing behavioural adaptation. *Nature*. 488:218–221.

Siegle JH, López AC, Patel YA, Abramov K, Ohayon S, Voigts J. 2017. Open Ephys: an open-source, plugin-based platform for multichannel electrophysiology. *J Neural Eng*. 14:045003.

Steinmetz NA, Aydin C, Lebedeva A, Okun M, Pachitariu M, Bauza M, Beau M, Bhagat J, Böhm C, Broux M, et al. 2020. Neuropixels 2.0: a miniaturized high-density probe for stable, long-term brain recordings. *bioRxiv*. doi: 10.1101/2020.10.27.358291.

Stuart GJ, Spruston N. 2015. Dendritic integration: 60 years of progress. *Nat Neurosci*. 18:1713–1721.

Suzuki M, Larkum ME. 2017. Dendritic calcium spikes are clearly detectable at the cortical surface. *Nat Commun*. 8:1–10.

Takata N, Hirase H. 2008. Cortical layer 1 and layer 2/3 astrocytes exhibit distinct calcium dynamics in vivo. *PLoS One*. 3: e2525.

Trainito C, Nicolai CV, Miller EK, Siegel M. 2019. Extracellular spike waveform dissociates four functionally distinct cell classes in primate cortex. *Curr Biol*. 29:1–10.

Travis KE, Leonard MK, Chan AM, Torres C, Sizemore ML, Qu Z, Eskandar E, Dale AM, Elman JL, Cash SS, et al. 2013. Independence of early speech processing from word meaning. *Cereb Cortex*. 23:2370–2379.

Truccolo W, Friehs GM, Donoghue JP, Hochberg LR. 2008. Primary motor cortex tuning to intended movement kinematics in humans with tetraplegia. *J Neurosci*. 28:1163–1178.

Uguz I, Ganji M, Adel H, Atsunori T, Inal S, Ahmed Y, Owens RM, Quilichini PP, Ghestem A, Christophe B, et al. 2016. Autoclave sterilization of PEDOT:PSS electrophysiology devices. *Adv Healthc Mater*. 5:3094–3098.

Ulbert I, Halgren E, Heit G, Karmos G. 2001a. Multiple microelectrode-recording system for human intracortical applications. *J Neurosci Methods*. 106:69–79.

Ulbert I, Heit G, Madsen J, Karmos G, Halgren E. 2004. Laminar analysis of human neocortical interictal spike generation and propagation: current source density and multiunit analysis in vivo. *Epilepsia*. 45:48–56.

Ulbert I, Karmos G, Heit G, Halgren E. 2001b. Early discrimination of coherent versus incoherent motion by multiunit and synaptic activity in human putative MT+. *Hum Brain Mapp*. 13:226–238.

Vigneswaran G, Kraskov A, Lemon RN. 2011. Large identified pyramidal cells in macaque motor and premotor cortex exhibit "thin spikes": implications for cell type classification. *J Neurosci*. 31:14235–14242.

Viventi J, Kim DH, Vigeland L, Frechette ES, Blanco JA, Kim YS, Avrin AE, Tiruvadi VR, Hwang SW, Vanleer AC, et al. 2011. Flexible, foldable, actively multiplexed, high-density electrode array for mapping brain activity in vivo. *Nat Neurosci*. 14:1599–1605.

Wang C, Ulbert I, Schomer DL, Marinkovic K, Halgren E. 2005. Responses of human anterior cingulate cortex microdomains to error detection, conflict monitoring, stimulus-response mapping, familiarity, and orienting. *J Neurosci*. 25: 604–613.

Waziri A, Schevon CA, Cappell J, Emerson RG, McKhann GM, Goodman RR. 2009. Initial surgical experience with a dense cortical microarray in epileptic patients undergoing craniotomy for subdural electrode implantation. *Neurosurgery*. 64:540–545.

Wilks SJ, Woolley AJ, Ouyang L, Martin DC, Otto KJ. 2011. In vivo polymerization of poly(3,4-ethylenedioxythiophene) (PEDOT) in rodent cerebral cortex. *Annu Int Conf IEEE Eng Med Biol Soc*. 2011:5412–5.

Yildirim M, Sugihara H, So PTC, Sur M. 2019. Functional imaging of visual cortical layers and subplate in awake mice with optimized three-photon microscopy. *Nat Commun*. 10: 177.

Zaitsev AV, Povysheva NV, Gonzalez-Burgos G, Rotaru D, Fish KN, Krimer LS, Lewis DA. 2009. Interneuron diversity in layers 2-3 of monkey prefrontal cortex. *Cereb Cortex*. 19:1597–1615.